Coupling network synthesis and modeling for microscopic understanding of strength in entangled polymer networks

Jinyue Dai[a], Xinyan Yang[a], Sinan Keten[a,b], Junsoo Kim[a,*]

[a] *Mechanical Engineering, Northwestern University, Evanston, 60208, IL, USA*
[b] *Civil Engineering, Northwestern University, Evanston, 60208, IL, USA*

Abstract

The strength of polymer networks, the maximum stress under uniaxial tension, arises from the collective loading and failure of heterogeneous polymer strands. However, its microscopic origins remain difficult to identify because network topology and strand-level forces cannot be directly resolved experimentally. Here, we combine experiments using polyacrylamide hydrogels as a model system with simulations using a mesoscale network model to determine how network structures govern strength. By varying precursor stoichiometry and degree of swelling, we systematically control the average strand length, entanglement-to-crosslink ratio, and strand prestretch. The model explicitly distinguishes crosslinks from entanglements and accounts for strand-length polydispersity, nonlinear elasticity, strand scission, and detanglement. We identify the strand density and the homogeneity of load distribution as two general descriptors of strength that apply across different network structures. Stronger networks maintain a sufficiently large population of load-bearing strands while distributing load more uniformly among them, thereby delaying localized strand scission and detanglement. Our approach combining experiments and modeling establishes a framework that relates microscopic mechanics to macroscopic fracture, which can guide a rational design of stronger polymer networks.

Keywords: Strength, Polymer networks, Network model, Entanglements

1. Introduction

Elastomers, gels, adhesives, and many soft biological tissues are networks of polymer chains constrained by crosslinks and entanglements. Their tensile strength determines the maximum load they can support and is therefore important for both engineering design and biological function. Although the elasticity of polymer networks has been extensively studied using statistical-mechanical theories [1–3], their ultimate tensile strength, the maximum stress under uniaxial tension, remains less predictable due to the lack of understanding of the underlying mechanism. This stress is carried collectively by polymer strands, defined as segments of polymer chains between neighboring crosslinks or entanglements. Strength therefore depends not only on the force required to break one strand, but also on how

*Corresponding author.
Email address: junsoo.kim@northwestern.edu

many strands carry load and how that load is redistributed when local damage occurs. This question differs from, although it can be related to, the energy-based description of crack growth. The Lake–Thomas model and its later extensions describe fracture energy by considering the energy released by strands near a crack plane [4–7]. Recent studies have also related crack propagation to the local strength near a crack tip [8, 9]. These theories connect strength with fracture behavior but do not explain how the strength is determined at the network scale. A separate body of work has examined the strength in terms of force distribution in the network. For example, Bueche proposed that scission of one strand transfers load to neighboring strands, followed by further strand scissions [10]. Later models predicted that only a small fraction of strands had broken at the peak stress and the macroscopic load was carried primarily by a limited number of highly extended polymer strands [11, 12]. These theoretical and modeling works do not, however, identify which features of network structure affect this load transfer and how changes in those features further alter strength.

One of the challenges in studying strength is that typical polymer networks are highly heterogeneous at the network level. Random crosslinking produces strands with different lengths, initial conformations, and junction functionality, together with defects such as loops and dangling ends [13–15]. As a result, strands in a polymer network subjected to uniform macroscopic deformation can carry very different forces. Tehrani and Sarvestani showed that shorter strands reach their limiting extension and break first, after which their load is redistributed to longer strands [13]. Statistical models have considered variations in chain configuration and the probability of scission to describe the progressive loss of strands [16, 17]. More recently, Tao et al. used an idealized model of chains loaded in parallel and showed that even a small variation in strand length can greatly reduce strength because short strands become highly loaded while longer strands still carry much smaller forces [18]. Simulations representing individual strands, also called discrete-network models, have further shown that loops, dangling ends, crosslinking heterogeneity, and non-affine deformation can affect strength and stretchability [14, 19–21]. However, the complexity of network heterogeneity makes it difficult to determine how these structural variations collectively govern strength.

Among the features of a polymer network, crosslinks and entanglements are two fundamental network structures because they establish the load-bearing paths within the polymer network. Both constrain chain motion, but in different ways. A crosslink permanently joins polymer chains. An entanglement prevents chains from passing through one another but allows them to slide relative to the point of entanglement. Previous experiments have shown that increasing crosslink density generally increases stiffness but does not necessarily increase strength [22–25]. The role of entanglements in strength has received less attention. Kim et al. prepared networks in which entanglements greatly outnumber crosslinks and showed that highly entangled hydrogels could reach tensile strengths approximately one order of magnitude greater than conventionally crosslinked comparison networks [26]. The improvement was attributed to long chains transmitting force through many entanglements, while the sparse crosslinks prevented complete disentanglement. Most studies of entanglements in polymer networks, however, have focused on fracture energy and fatigue rather than the strength [5, 26–30]. For example, Zheng et al. showed that entangled networks can exhibit fracture toughness much greater than their fatigue threshold despite limited bulk hysteresis and attributed this difference to chain pullout and distributed damage near the crack tip [28].

However, fracture energy and strength characterize fundamentally different processes: fracture energy quantifies resistance to the propagation of an existing crack, whereas strength is a measure of crack nucleation in a flaw-insensitive sample [31]. Understanding strength therefore requires tracking how load is distributed before macroscopic failure begins. Such tracking remains experimentally challenging because the current spatiotemporal resolution of existing microscopy and force spectroscopy cannot resolve network structure or the forces carried by individual strands.

Alternatively, computational modeling provides a complementary approach for investigating the underlying mechanism of strength. Computational modeling has been developed at distinct length scales, such as the atomic or continuum scales. Continuum and finite-element models address macroscopic deformation efficiently, including crack propagation, but they generally use constitutive variables and cannot explicitly capture the forces carried by individual strands [17, 32–34]. Atomistic and coarse-grained molecular simulations provide much greater molecular details, including chain conformation, entanglement formation, chain pullout, and bond scission, but the accessible size of systems and deformation rates often limit direct comparisons with macroscopic experimental results [35–37]. Network-scale models bridge two length scales by modeling individual strands and junctions as springs and nodes [38, 39]. Previous network models show that failure depends strongly on network heterogeneity and load redistribution [11, 19, 21, 40]. Hanson and Barber related strength to crosslink density and initial chain conformation and found that fewer than 1% of strands had broken at peak stress [11]. Tauber et al. further demonstrated that nonuniform load redistribution controls damage and the macroscopic response of double networks [40]. Entanglement models have primarily focused on load redistribution through sliding [41–43]. Assadi et al. showed that changes in the entanglement population govern non-affine deformation and nonlinear rheology [41]. Huang et al. showed that sliding equalizes tension among strand segments, thereby increasing network strength and reducing stress concentration near a crack [42]. Overall, these studies separately examine the effects of crosslinks and entanglements on strength, leaving their combined structure-property relation unresolved. A model that distinguishes entanglements from crosslinks while capturing the evolution of damage is therefore needed to determine how they jointly govern strength.

In this work, we establish an experimental and computational framework to investigate how network structure governs the strength of polymer networks. In experiments, we use polyacrylamide hydrogels as a model system and control the stoichiometry of precursor and swelling ratio after synthesis to vary network structural variables, including average strand length, entanglement-to-crosslink ratio, and prestretch of strands. In parallel, we develop a two-dimensional network model as a reduced representation of an isotropic three-dimensional polymer network. This model treats crosslinks and entanglements as nodes without and with chain slip, respectively. Polymer strands are represented as springs connecting these nodes, with forces governed by nonlinear chain elasticity. The model accounts for variations in polymer strand length, finite extensibility with strand scission, and pullout of free strand ends. The experiments characterize the macroscopic mechanical response and show agreement with the model predictions, while the model further reveals the underlying evolution of load redistribution and damage. We find that the three structural variables above jointly affect strand density, remaining extensibility, and entanglement-mediated load redistribution, which are strongly correlated with the strength. Statistical analysis shows that stronger

networks combine a higher population of strands and more uniform load distribution among them, thereby delaying localized scission and junction loss. This framework provides a microscopic basis for relating network structure to strength and offers principles for designing strong polymer networks.

2. Experiments

We consider polymer networks that are synthesized by polymerizing monomers with crosslinkers (Fig. 1A). As a model system, we choose polyacrylamide (PAAm) hydrogels because their nearly elastic behavior allows us to study the effects of network structure with minimal influence from bulk viscoelasticity [26]. The precursor composition is specified by the water-to-monomer molar ratio W and the crosslinker-to-monomer molar ratio C. Increasing C increases the density of crosslinks and decreases the average strand length between them. Decreasing W increases the monomer concentration during polymerization and promotes the formation of entanglements [26]. Crosslinks trap some entanglements within the network, fixing the network topology (Fig. 1A and B). The rest of the entanglements remain as transient entanglements. We assume that they would eventually detangle upon deformation, particularly at low stretch rates, and not contribute to strength. Subsequent swelling decreases the number density of polymer strands and increases their average end-to-end distance, where we define a swelling-induced prestretch λ_p (Fig. 1C). These three preparation variables, C, W and λ_p, together determine the network structures before deformation. Next, we apply uniaxial tension with stretch λ referenced to the swollen state (Fig. 1D). We hypothesize that the strength originates from the network structures that induce inhomogeneous tension distribution.

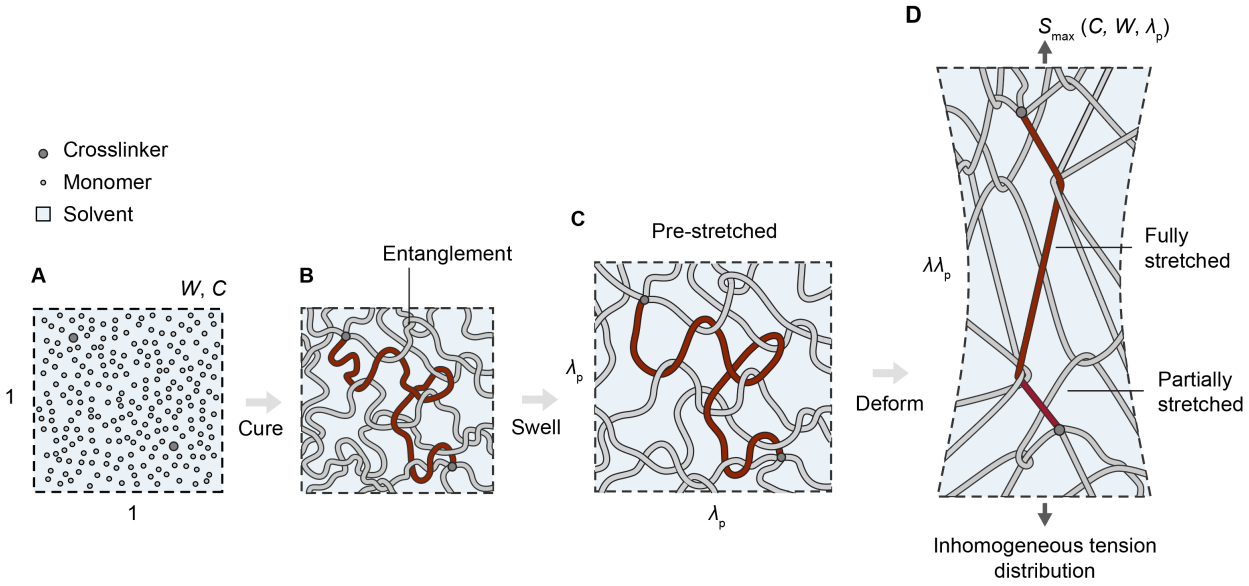


Figure 1: Preparation–structure–strength relationship of polymer networks investigated in this work. (A) The precursor composition is controlled by the water-to-monomer molar ratio W and crosslinker-to-monomer molar ratio C. (B) Polymerization produces a network containing crosslinks and trapped entanglements. (C) Swelling decreases the strand density and produces a swelling-induced prestretch λ_p. (D) Under uniaxial tension with a stretch λ from the swollen state, the macroscopic nominal strength $S_{\max}(C, W, \lambda_p)$ arises from an inhomogeneous distribution of strand extension and load bearing.

All chemicals were used as received, including acrylamide (AAm; Sigma–Aldrich, A8887), N, N'-methylenebisacrylamide (MBAA; Sigma–Aldrich, M7279), 2-hydroxy-4'-(2-hydroxyethoxy)-2-methylpropiophenone (Irgacure 2959; Sigma–Aldrich, 410896), and ethanol (Sigma–Aldrich, E7023). Deionized water was obtained from an in-house purification system. The aqueous precursor contained AAm as the monomer, MBAA as the crosslinker, Irgacure 2959 as the photoinitiator, and water as the solvent. For precursors with low W, the concentrated aqueous AAm solution was heated in a microwave oven for approximately 15 s to fully dissolve the monomer before MBAA was added. Because Irgacure 2959 is poorly soluble in water, it was dissolved separately in ethanol at a concentration of 0.1 M. The aqueous AAm–MBAA solution and the initiator solution were then mixed. We maintained $I/C = 0.4$ for all formulations, where I is the initiator-to-monomer molar ratio, so that the fraction of dangling strands to load-bearing strands is negligible, and the mechanical response can be attributed primarily to W and C. The effect of varying I/C on mechanical properties was reported previously [26]. The resulting precursor solutions were cast and photopolymerized under UV light at an intensity of 1.5 mW/cm^2 for 3 h to form PAAm hydrogel sheets. Neglecting the small mass contributions of the crosslinker and initiator solution, the polymer content ϕ_{init} in the as-prepared state is determined directly by W: $\phi_{\text{init}} = M_{\text{m}}/(M_{\text{m}} + WM_{\text{s}})$, where M_{m} and M_{s} are the molar masses of the monomer and solvent, respectively.

After synthesis, we can further vary the polymer content by swelling. To reach a specific polymer content, we controlled the amount of absorbed water, after which the specimens were sealed and allowed to homogenize before testing. Hydrogels designated for equilibrium swelling were submerged in a sufficient amount of water for at least 24 h. We weighed the as-

prepared and swollen samples, and calculated the swelling ratio J_p. Assuming isotropic three-dimensional swelling, the experimental prestretch $\lambda_{p,\mathrm{exp}}$ induced by swelling was calculated as $\lambda_{p,\mathrm{exp}} = J_p^{1/3}$. Therefore, $\lambda_{p,\mathrm{exp}} = 1$ denotes an as-prepared hydrogel, whereas $\lambda_{p,\mathrm{exp}} > 1$ denotes a swollen hydrogel with prestretched strands.

Hydrogel sheets were cut into dumbbell-shaped specimens using a metal die (ISO 37, Type 4). Uniaxial tensile tests were performed using an Instron 34TM30 equipped with a 50 N load cell. The specimens were loaded to fracture at a constant engineering strain rate of 0.1 s^{-1}. Over the range relevant to this study, the tensile response of PAAm hydrogels is weakly dependent on the loading rate [26]. Five specimens were tested for each preparation condition. Nominal stress S was calculated by dividing the measured force by the undeformed cross-sectional area, and stretch λ was calculated as the ratio of the current gauge length to its undeformed value. Strength S_{max} was defined as the maximum nominal stress, and the corresponding stretch, or stretchability, was denoted by λ_{max}. The modulus was obtained from the initial slope of the nominal stress–stretch curve (up to stretch of 1.05). The work of fracture was calculated as the area under the nominal stress–stretch curve up to λ_{max}.

3. Network modeling

3.1. Physical representation of the polymer network

We develop a computational framework that models a polymer network consisting of crosslinks and entanglements. This network model is two-dimensional, which is a reduced representation of an isotropic three-dimensional network. This reduction in dimension can be rationalized as the in-plane response of a thin specimen under plane-stress conditions, such that the out-of-plane stress components are assumed to vanish, which has been known to be effective in capturing the mechanical behavior of different polymeric systems [38, 39].

To represent a polymer network, the network model uses nodes connecting polymer strands. Each node is designated either as a crosslink or an entanglement. A strand i connects nodes $a(i)$ and $b(i)$, and its end-to-end vector is

$$\mathbf{r}_i = \mathbf{x}_{b(i)} - \mathbf{x}_{a(i)}, \tag{1}$$

where $\mathbf{x}_{a(i)}$ and $\mathbf{x}_{b(i)}$ are the positions of the two terminal nodes. The strand length and contour length are

$$r_i = \|\mathbf{r}_i\|, \qquad L_{\mathrm{c},i} = N_{\mathrm{K},i} b, \tag{2}$$

respectively, where $N_{\mathrm{K},i}$ is the number of Kuhn segments assigned to strand i, and b is the Kuhn length.

When the forces on the strands connecting to a node are imbalanced, the node moves in response to the resultant force (Fig. 2A–B). The resultant force acting on a node j, $\mathbf{f}_j^{\mathrm{res}}$, is a summation of the tensile force exerted by connected strands, $\mathbf{f}_j^{\mathrm{L}}$, and the repulsive force between nodes, $\mathbf{f}_j^{\mathrm{R}}$, that prevent unphysical collapse and overlap of neighboring nodes to establish a finite equilibrium separation. Since the repulsive force is negligible when the nodes are far from each other, we only consider pairwise nodes within a certain cutoff distance. Thus, the resultant force acting on a node j is

$$\mathbf{f}_j^{\mathrm{res}} = \sum_{i \in \mathcal{C}(j)} \mathbf{f}_j^{\mathrm{L},i} + \sum_{q \in \mathcal{R}(j)} \mathbf{f}_j^{\mathrm{R},jq}, \tag{3}$$

where $\mathcal{C}(j)$ is the set of strands connected to node j, and $\mathcal{R}(j)$ is the set of neighboring nodes within the cutoff distance. Then, the node j will move in the direction of $\mathbf{f}_j^{\text{res}}$. The details of force convergence are described in Appendix A.3.

While crosslink nodes and entanglement nodes are identically modeled in terms of translation, they are differently modeled in terms of chain slip. Crosslinks act as permanent junctions without chain slip, whereas entanglements act as slip-links [44, 45]. Each entanglement joins two primitive paths, represented as four strands connected by an entanglement node (Fig. 2B). A slip event transfers one Kuhn segment between adjacent strands along each participating primitive path. For the slip direction shown in Fig. 2B,

$$(n_1, n_2, n_3, n_4) \longrightarrow (n_1 + 1, n_2 - 1, n_3 - 1, n_4 + 1), \tag{4}$$

so that the total number of Kuhn segments in each primitive path is conserved. The transfer direction is determined by the local imbalance in strand loading. Slippage is treated as a thermally activated process with a rate according to the Eyring kinetic theory (see Appendix A.1 for details).

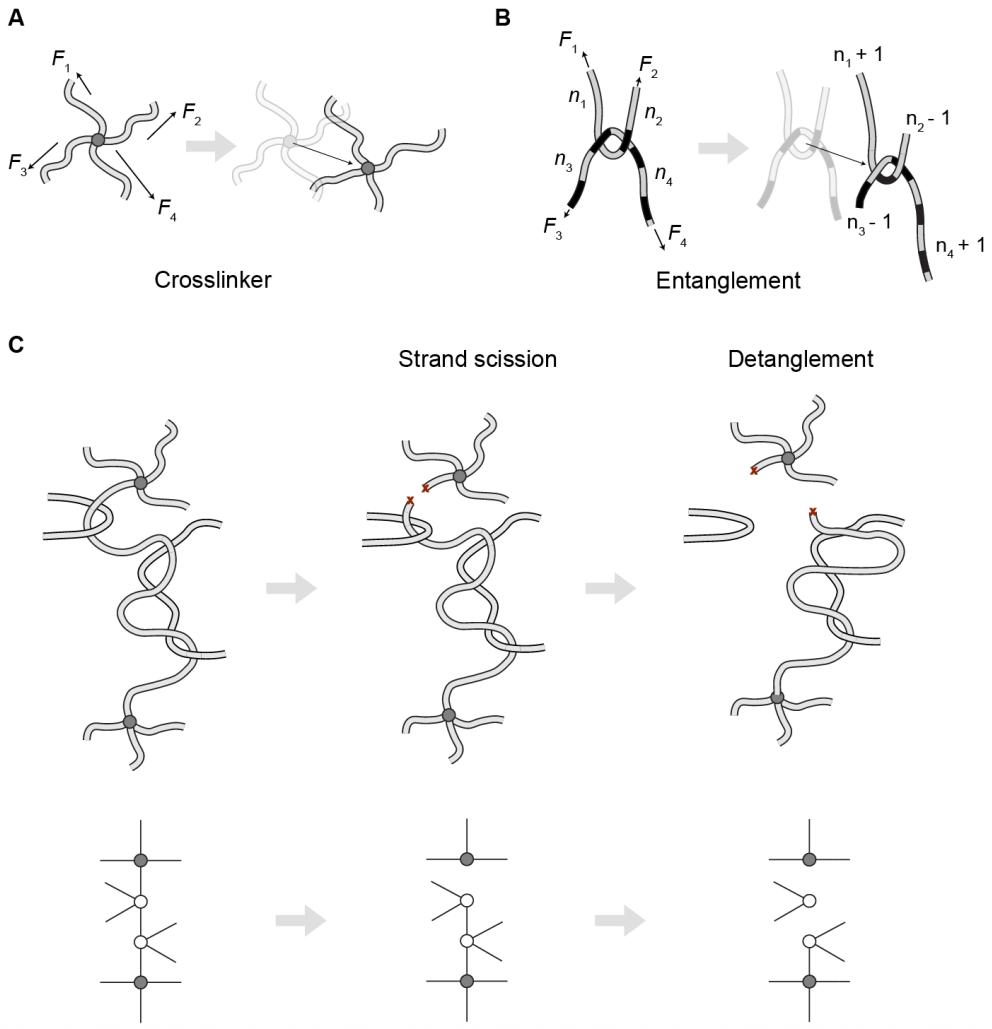


Figure 2: Schematic representation of network junctions and damage mechanisms. (A) Crosslinks are represented as permanent junctions that transmit forces among connected strands. (B) Entanglements are represented as slip-links that redistribute contour length among strands in a primitive path. (C) Strand scission and detanglement modify the network connectivity during deformation. Strand scission removes a load-bearing strand, whereas detanglement removes a strand after sufficient contour-length slipout. The diagrams below illustrate the corresponding changes in network connectivity, with gray circles denoting crosslink nodes and white circles denoting entanglement nodes.

Two irreversible damage mechanisms, which modify the topology, are incorporated: strand scission and detanglement. Strand i breaks when the strand end-to-end distance r_i reaches the prescribed threshold, which is set to be 98% of its contour length. Correspondingly, we define a proximity-to-scission index as

$$\eta_i = \frac{r_i}{0.98 L_{\mathrm{c},i}}, \tag{5}$$

such that $\eta_i = 1$ denotes the threshold of strand scission. Once this condition is met, the strand breaks and splits into two free ends. A free end adjacent to an entanglement can continue to slip until it passes completely through the junction, at which point the entanglement

node is deleted. Thus, strand scission directly removes one load-bearing connection, whereas detanglement results from the subsequent slipout of a free end (Fig. 2C). Detailed computational approaches to track the contour length and network connectivity are described in Appendix A.1.

We model the mechanical behavior of an individual polymer strand based on the freely jointed chain model with finite extensibility [46, 47] (Fig. 3A):

$$f^{\mathrm{L}}(r_i) = \frac{k_{\mathrm{B}}T}{b}\mathcal{L}^{-1}\left(\frac{r_i}{L_{\mathrm{c},i}}\right), \tag{6}$$

where f^{L} is the tensile force of the strand, $\mathcal{L}^{-1}$ denotes the inverse Langevin function, $k_{\mathrm{B}}T$ is the temperature in unit of energy, b is the Kuhn length. For a given strand i, $\mathbf{f}^{\mathrm{L},i} = f^{\mathrm{L}}(r_i)\mathbf{r}_i/\|\mathbf{r}_i\|$ and $L_{\mathrm{c},i}$ is a constant. When r_i is small, the force carried by a strand is dominated by its entropic motion without considering the excluded volume, resulting in positive tension in the entire stretch range. As r_i approaches $L_{\mathrm{c},i}$, the force diverges. Note that the force substantially develops before divergence when the strands are long. If we set the scission threshold in terms of force, long strands would break too early, so we choose the scission threshold in terms of $r_i/L_{\mathrm{c},i}$ (Eq. 5).

Since the Langevin-chain model does not consider the excluded volume of strands, we further consider the repulsive force. For two nodes separated by the pairwise distance d, the repulsive force f^{R} with a cutoff distance R_c is described as

$$f^{\mathrm{R}}(d) = \begin{cases} \epsilon\gamma\left(\dfrac{1}{R_c} - \dfrac{R_c^{\gamma}}{d^{\gamma+1}}\right), & d < R_c, \\ 0, & d \geq R_c, \end{cases} \tag{7}$$

where ϵ is a characteristic energy scale that determines the magnitude of the repulsion and γ represents how rapidly the repulsion decays. Here, γ is set to 2 in order to achieve a soft pairwise repulsion (12 for common Lennard–Jones repulsion). The parameter ϵ is set such that the net force between two nodes can be approximately zero at $d = r_0$, where r_0 is the initial end-to-end distance of the strand connecting the nodes. This suggests that the networks host some effective pressure at the initial state due to volume exclusion. The Langevin interaction acts only between the two end nodes of a strand, whereas the repulsive interaction acts between every pair of nodes separated by less than R_c. The fixed interaction parameters are listed in Table A.1 in Appendix A.4.

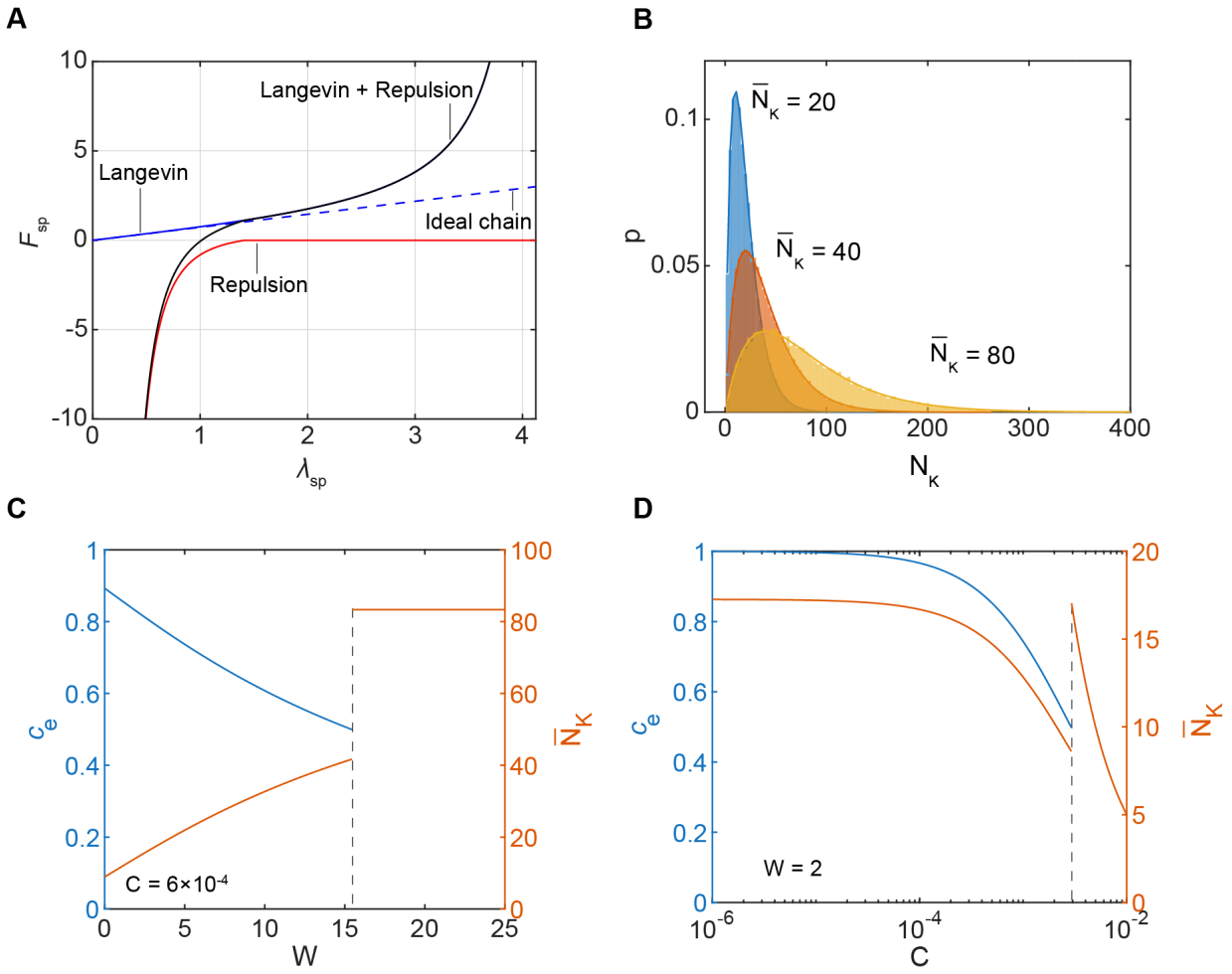


Figure 3: Constitutive forces of polymer strands and parameterization of network structure. (A) Force–stretch relation of a single polymer strand with Langevin elasticity and short-range repulsion. (B) Probability distributions for representative values of mean strand length $\overline{N}_{\mathrm{K}}$ at $PDI = 1.5$. (C) Dependence of entanglement fraction c_e and $\overline{N}_{\mathrm{K}}$ on the water-to-monomer ratio W at $C = 6 \times 10^{-4}$. (D) Dependence of c_e and $\overline{N}_{\mathrm{K}}$ on C at $W = 2$. Dashed lines mark the transition between the entangled regime and the unentangled regime.

Network heterogeneity is introduced through a distribution of the number of Kuhn segments per strand (Fig. 3B). Each $N_{\mathrm{K},i}$ is sampled from the Schulz–Zimm distribution [48, 49]:

$$p(N_{\mathrm{K}}) = \frac{\alpha^{\alpha}}{\Gamma(\alpha)\overline{N}_{\mathrm{K}}^{\alpha}} N_{\mathrm{K}}^{\alpha-1} \exp\left(-\alpha \frac{N_{\mathrm{K}}}{\overline{N}_{\mathrm{K}}}\right), \tag{8}$$

where $\overline{N}_{\mathrm{K}}$ is the prescribed mean, α controls the relative breadth, and $\Gamma(\alpha)$ is the Gamma function. We set $\alpha = 2$, corresponding to a representative polydispersity index (PDI) $= 1 + \alpha^{-1} = 1.5$.

3.2. Mapping experimental preparation variables to network modeling parameters

The experimental preparation variables C, W, and $\lambda_{p,\mathrm{exp}}$ are mapped onto three parameters of the simulated network: the mean number of Kuhn segments per strand $\overline{N}_{\mathrm{K}}$, the

fraction of entanglement nodes c_e, and the initial dilation of the two-dimensional network λ_p. The mean number of Kuhn segments between neighboring crosslinks is calculated from C as

$$N_c = \frac{1}{2Cn_{\mathrm{K}}}, \tag{9}$$

where n_{K} is the number of monomers per Kuhn segment. The factor of two accounts for the fact that a crosslink connects four strands and a strand requires two crosslinks. Here, we assume $n_{\mathrm{K}} = 10$ for polyacrylamide. The characteristic entanglement length N_e is modeled as [50]

$$N_e = N_e^0 \phi_{\mathrm{init}}^{-4/3}, \tag{10}$$

where N_e^0 is the reference entanglement length in terms of Kuhn segments in the dry state, and ϕ_{init} is the initial polymer fraction at as-prepared state [50]. Specifically, N_e^0 is set to 10 based on the entanglement molecular weight of dry polyacrylamide melt from the literature [51]. Recall that $\phi_{\mathrm{init}} = M_{\mathrm{m}}/(M_{\mathrm{m}} + WM_{\mathrm{s}})$. For example, $W = 2$ gives $\phi_{\mathrm{init}} \simeq 0.66$, corresponding to $N_e \simeq 17$ Kuhn segments.

When $N_e < N_c$, crosslinks and entanglements both subdivide the polymer contour into load-bearing strands. Assuming that the number density of Kuhn segments is constant, the number densities of entanglements and crosslinks are proportional to $1/N_e$ and $1/N_c$, respectively. The number density of all nodes is given as the sum of the number densities of crosslinks and entanglements. Therefore, $\overline{N}_{\mathrm{K}}$ can be calculated by the harmonic mean of N_c and N_e: $\overline{N}_{\mathrm{K}} = N_c N_e/(N_c + N_e)$. When $N_e > N_c$, we assume that strands do not entangle due to dense crosslinks. Therefore, $\overline{N}_{\mathrm{K}}$ and c_e are defined as

$$\overline{N}_{\mathrm{K}} = \begin{cases} \dfrac{N_c N_e}{N_c + N_e}, & N_e < N_c, \\ N_c, & N_e \geq N_c, \end{cases} \tag{11}$$

and

$$c_e = \begin{cases} \dfrac{1/N_e}{(1/N_c) + (1/N_e)} = \dfrac{N_c}{N_c + N_e}, & N_e < N_c, \\ 0, & N_e \geq N_c. \end{cases} \tag{12}$$

At fixed C, increasing W lowers the polymer content ϕ_{init} during network formation, increases N_e and $\overline{N}_{\mathrm{K}}$, and reduces c_e until the unentangled regime is reached (Fig. 3C). At fixed W, increasing C decreases N_c, shortens the strands, and changes the network from entanglement-dominated toward crosslink-dominated (Fig. 3D).

3.3. Network preparation and loading

We establish an initial configuration of the polymer network, and let it reach equilibrium before applying the deformation. For the initial configuration, nodes are placed on a rhombic lattice and each node connects four strands (Fig. 4A). We apply a periodic boundary condition on a primary cell (colored) with its replicas (gray). The number of Kuhn segments in each strand is then assigned using Eq. (8), a fraction c_e of the total nodes is designated as entanglements, and the remaining nodes are designated as crosslinks. The initial network topology contains neither loops nor dangling ends, which will not be studied in the present

model. Details of the network construction, periodic boundaries, and system-size convergence are provided in Appendix A.2. The initial lattice spacing is taken as the initial strand end-to-end distance r_0, which can be estimated as the root-mean-square of the end-to-end length for a representative strand of $\overline{N}_{\mathrm{K}}$ [50]:

$$r_0 = b\overline{N}_{\mathrm{K}}^{\frac{1}{2}}. \tag{13}$$

This distance r_0 represents the characteristic coil size of the strands. After the lengths $N_{\mathrm{K},i}$ are assigned to individual strands, the nodes are under force imbalance due to the nonuniform distribution of strand lengths. Before imposing any deformation, the as-generated network is first equilibrated until the average magnitude of residual forces over all nodes satisfies the prescribed convergence criterion (Appendix A.3). The initial lattice structure becomes irregular while preserving its connectivity (Fig. 4B).

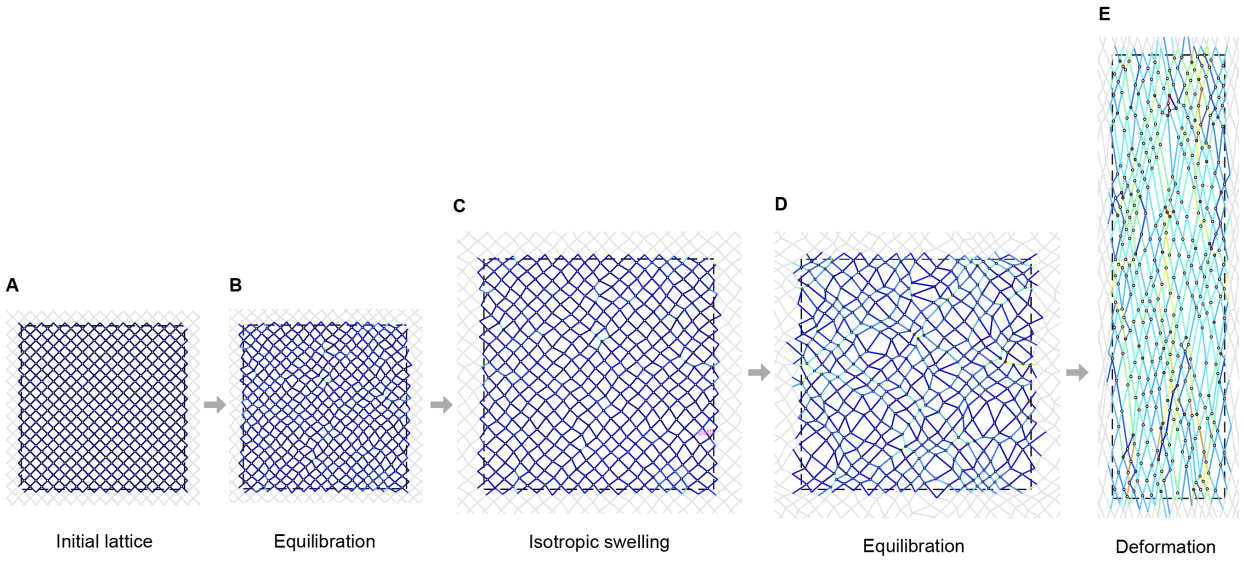


Figure 4: Network preparation and loading protocol. (A) Initial periodic rhombic lattice. (B) Mechanical equilibrium of initial network. (C) Isotropic dilation to represent swelling. (D) Re-equilibrated swollen network. (E) Network under uniaxial deformation. The replicas of the primary cell under periodic boundary condition are shown in light gray. Strand colors indicate the force level on strands.

Next, we consider swelling of the equilibrated network (Fig. 4C). Swelling is modeled as a two-dimensional isotropic dilation:

$$\mathbf{F}_p = \lambda_p \mathbf{I}, \tag{14}$$

which transforms the coordinates of nodes from $\mathbf{x}_j$ to $\mathbf{F}_p\mathbf{x}_j$ and linearly scales the dimensions of primary cell L_x and L_y by λ_p. Consequently, the area of the cell changes from initial area A_{init} to swollen area A_p by λ_p^2. Denote ϕ as the polymer content after swelling. While the three-dimensional experimental relation relates $\lambda_{p,\mathrm{exp}}^3 = \phi_{\mathrm{init}}/\phi$, under two-dimensional approximation, we set $\lambda_p^2 = \phi_{\mathrm{init}}/\phi$. After dilation, the network is re-equilibrated at fixed cell dimensions, which will serve as the reference configuration with $A_{\mathrm{ref}} = A_p$ for subsequent deformation (Fig. 4D).

Next, uniaxial tension is applied along the y-direction (Fig. 4E). Within the two-dimensional representation, the area is fixed during deformation to impose the incompressibility. The imposed deformation gradient is given as

$$\mathbf{F}(\lambda) = \begin{bmatrix} \lambda^{-1} & 0 \\ 0 & \lambda \end{bmatrix}, \tag{15}$$

where λ is the stretch relative to the reference configuration. Note that $\det \mathbf{F} = 1$ as the area of the cell is fixed. At each loading increment, we update the dimensions of the periodic cell and coordinates of nodes proportional to the macroscopic deformation (i.e., affine deformation); let the strands slip and break; and re-equilibrate the network. The precise order of update, numerical integration, and convergence criteria are given in Appendix A.3.

3.4. Mechanical descriptors

The virial stress of the simulated network is calculated from the strand forces and current end-to-end vectors:

$$\boldsymbol{\sigma}^v = \frac{1}{A} \sum_{i \in \mathcal{A}} \mathbf{f}_i^L \otimes \mathbf{r}_i, \tag{16}$$

where A is the current network area, $\mathcal{A}$ is the set of active strands in the primary cell, and $\mathbf{f}_i^L$ and $\mathbf{r}_i$ are the Langevin force vector and end-to-end vector of strand i, respectively. The network area remains constant during loading, so $A = A_{\text{ref}}$, where A_{ref} is the area of the equilibrated reference configuration.

The tensile component of the virial stress along the loading direction y is

$$\sigma_{yy}^v = \frac{1}{A_{\text{ref}}} \sum_{i \in \mathcal{A}} f_{i,y}^L r_{i,y}. \tag{17}$$

The nominal tensile stress is then obtained by dividing this component by the stretch λ:

$$\sigma^v(\lambda) = \frac{\sigma_{yy}^v(\lambda)}{\lambda} = \frac{1}{A_{\text{ref}}} \sum_{i \in \mathcal{A}} V_i(\lambda), \qquad V_i(\lambda) = \frac{f_{i,y}^L(\lambda)\, r_{i,y}(\lambda)}{\lambda}, \tag{18}$$

where λ is measured relative to the equilibrated reference configuration. Here, V_i is the strand-level virial contribution to the nominal stress before area normalization. This definition separates individual strand loading from the density of strands.

The simulated nominal strength $\sigma_{\max}^v$ is defined as the maximum value of σ^v: $\sigma_{\max}^v = \sigma^v(\lambda_{\max})$, where its corresponding stretchability is denoted by $\lambda_{\max}$. The modulus is obtained from the initial slope of the nominal stress–stretch curve (up to stretch of 1.05). The work of fracture reported here is the area under the nominal stress–stretch curve from $\lambda = 1$ to $\lambda_{\max}$. The initial strand density is defined here as the number of strands per unit area in the reference configuration:

$$\nu_{\text{strand}} = \frac{N_{\mathcal{A},0}}{A_{\text{ref}}}, \tag{19}$$

where $N_{\mathcal{A},0}$ is the initial number of strands before uniaxial loading. Since the initial lattice spacing scales as $r_0 \propto \overline{N}_{\text{K}}^{1/2}$, the strand density at a fixed number of nodes scales as

$$\nu_{\text{strand}} \propto \frac{1}{\lambda_p^2 \overline{N}_{\text{K}}}. \tag{20}$$

Therefore, increasing either the mean strand length or the swelling-induced prestretch reduces the number density of load-bearing strands at the reference state.

The strand orientation relative to the loading direction is quantified by

$$\left\langle \cos^2\theta \right\rangle = \frac{1}{N_{\mathcal{A}}} \sum_{i\in\mathcal{A}} \left(\frac{r_{i,y}}{r_i} \right)^2, \tag{21}$$

where θ is the angle between the strand end-to-end vector and the loading direction and $N_{\mathcal{A}}$ is the current number of strands in set $\mathcal{A}$. In two dimensions, $\langle \cos^2\theta \rangle = 1/2$ refers to an isotropic orientation, and $\langle \cos^2\theta \rangle = 1$ refers to strand alignment with the loading direction.

The load distribution among the strands is characterized using the mean of V_i and its coefficient of variation:

$$\langle V \rangle = \frac{1}{N_{\mathcal{A}}} \sum_{i\in\mathcal{A}} V_i, \tag{22}$$

and

$$\mathrm{CV}_V = \frac{\sqrt{\langle (V - \langle V \rangle)^2 \rangle}}{\langle V \rangle}. \tag{23}$$

A larger CV_V indicates greater strand-to-strand variation relative to the mean load. To compare the shape of the load distributions among networks with different stress scales, the strand-level contribution can be further normalized as

$$\widetilde{V}_i = \frac{V_i}{\langle V \rangle}, \tag{24}$$

such that $\langle \widetilde{V} \rangle = 1$. Furthermore, we define V_{99} and V_{50} as V_i at the 99th percentile and 50th percentile among the strands. We characterize the relative upper tail of the distribution of V_i as V_{99}/V_{50}.

The cumulative events of strand scission and detanglement are normalized by $N_{\mathcal{A},0}$:

$$\phi_{\mathrm{scission}}(\lambda) = \frac{N_{\mathrm{scission}}(\lambda)}{N_{\mathcal{A},0}}, \qquad \phi_{\mathrm{detangle}}(\lambda) = \frac{N_{\mathrm{detangle}}(\lambda)}{N_{\mathcal{A},0}}, \tag{25}$$

where N_{scission} is the cumulative number of broken strands and N_{detangle} is the cumulative number of detangled strands. We denote their sum at peak stress as a damage index ϕ_{deletion}:

$$\phi_{\mathrm{deletion}}(\lambda) = \phi_{\mathrm{scission}}(\lambda) + \phi_{\mathrm{detangle}}(\lambda). \tag{26}$$

4. Results and discussion

4.1. Effect of crosslinker-to-monomer molar ratio C

We first vary the crosslinker-to-monomer molar ratio C while fixing the other preparation variables W and λ_p. Experimentally, PAAm hydrogels are synthesized at $W = 2$ with $C = 1.2 \times 10^{-5}$, 6×10^{-5}, 3×10^{-4}, 6×10^{-4}, 1.2×10^{-3}, or 3×10^{-3}, and are tested in the as-prepared state ($\lambda_{p,\mathrm{exp}} = 1$). Computationally, the values of C determine the mean number of Kuhn segments per strand, $\overline{N}_{\mathrm{K}}$, and the entanglement fraction, c_e, through Eqs. (11) and (12), respectively. The values of network structural parameters used are listed

in Table A.2. This series therefore changes not only the number of crosslinks but also the relative contributions of crosslinks and entanglements.

The experimental stress–stretch curves show that decreasing C generally increases both the strength and the stretchability (Fig. 5A). The simulated curves reproduce the same trend in C (Fig. 5B). We observe that the strength increases as C decreases in both experiments and simulations (Fig. 5C). The stretchability likewise increases as C decreases (Fig. 5D), leading to the similar trend in the work of fracture (Fig. 5E). As C increases, the experimental modulus shows no statistically significant change, and the change in simulated modulus is also small compared to orders of magnitude changes in C (Fig. 5F). We attribute this weak dependence to the contribution of entanglements, which outnumber crosslinks over the wide range of C examined. The contribution of crosslinks becomes more pronounced only at high C. Note that we refrain from comparing absolute values of stretch and stress between experimental and computational data, due to the assumptions and simplifications in the network model.

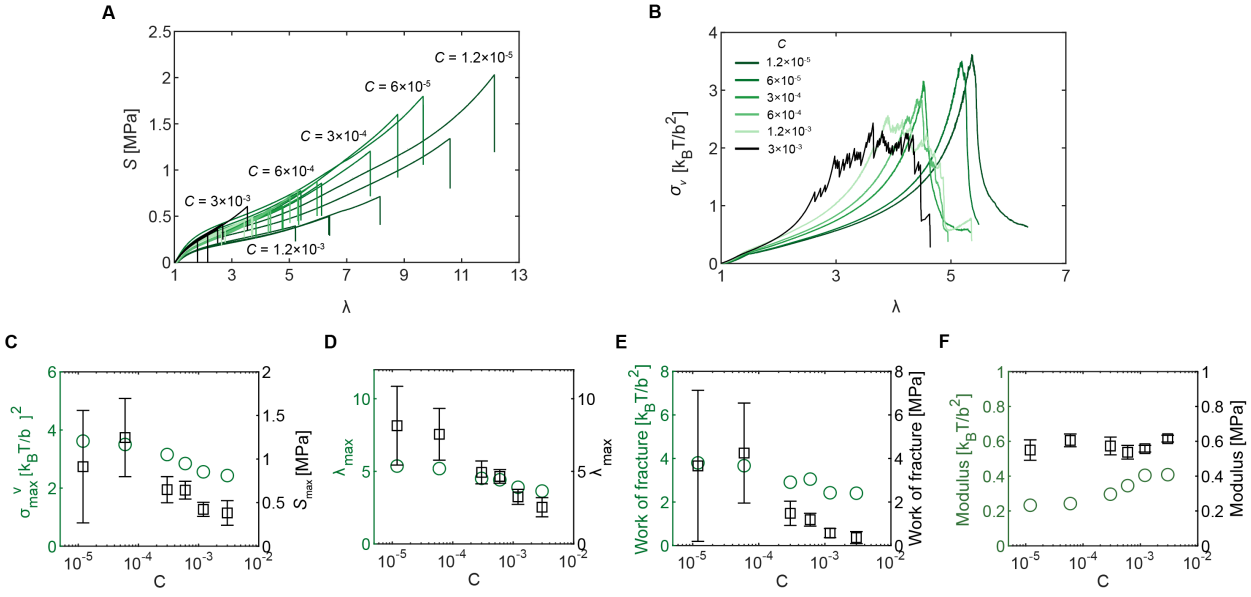


Figure 5: Effect of crosslinker-to-monomer molar ratio C on the stress–stretch curves under uniaxial tension at $W = 2$ in the as-prepared state. (A) Experimental nominal stress–stretch curves and (B) simulated nominal virial stress–stretch curves for networks with different C. (C–F) Strength, stretchability, work of fracture, and modulus as functions of C. Simulation results are shown in green and referenced to the left axes, whereas experimental measurements are shown in black and referenced to the right axes.

Next, we plot the network configurations at peak stress using coordinates normalized by the deformed cell dimensions. Although this normalization does not preserve the physical strand lengths and orientations, it enables detailed visualization at large stretches and direct comparison of networks with different dimensions (Fig. 6A). Each strand is colored by its proximity-to-scission index η_i. The value of η_i is linearly color-coded using the Jet colormap from 0 (blue) to 1 (red), thereby enabling the visualization of force distribution within the network. We consider three representative values of C. At $C = 3 \times 10^{-3}$ ($N_c < N_e$), the strands between crosslinks are too short to contain entanglements (Fig. 6A). At $C = 1.2 \times 10^{-3}$ ($N_c > N_e$), the network contains both crosslinks and entanglements. At $C = 1.2 \times 10^{-5}$

($N_c \gg N_e$), entanglements dominate the network. The three values of C show the transition from a crosslink-dominated network to an entanglement-dominated network.

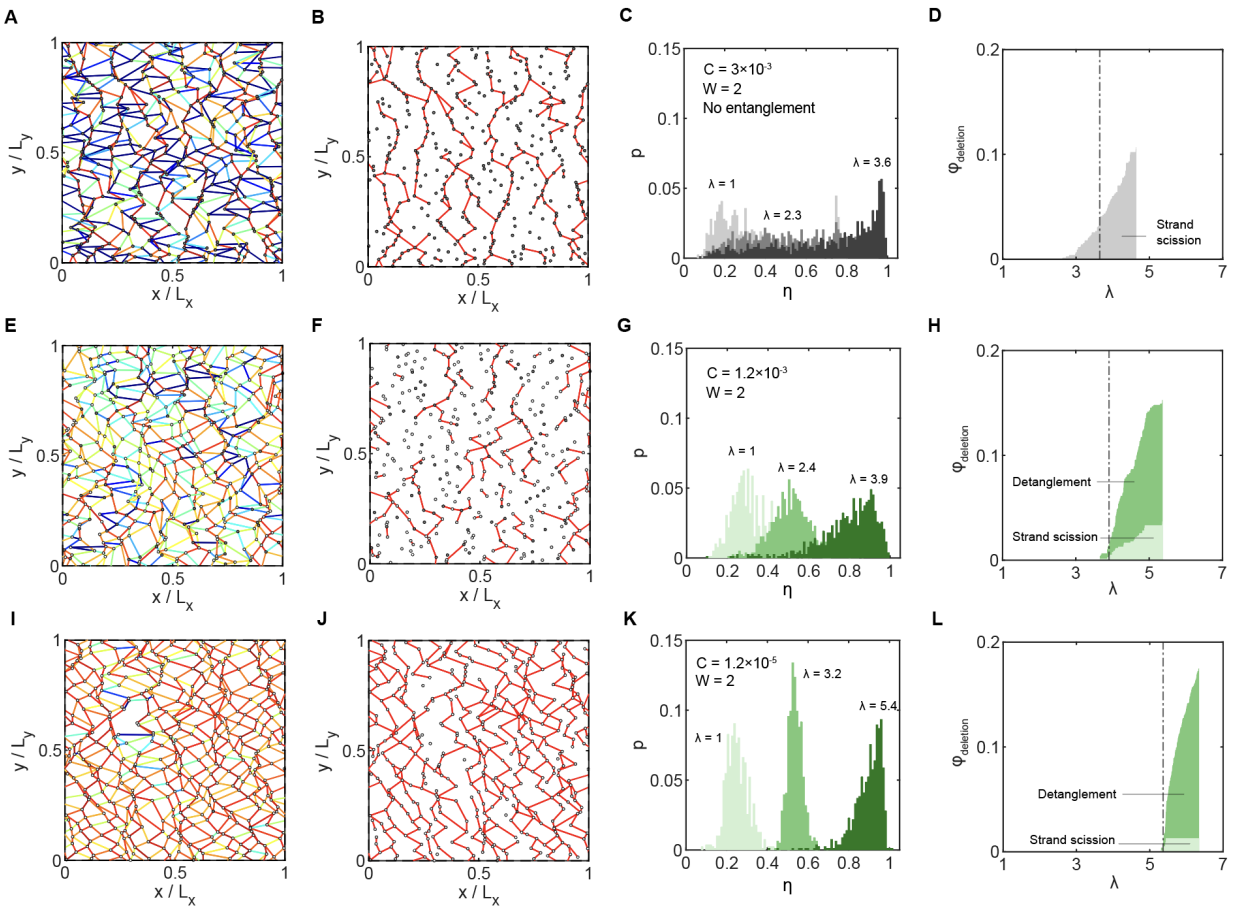


Figure 6: Network configuration and force distribution of networks with different crosslinker-to-monomer molar ratios C at fixed $W = 2$: (A–D) $C = 3 \times 10^{-3}$, (E–H) 1.2×10^{-3}, and (I–L) 1.2×10^{-5}. (A, E, I) Network configurations at peak stress, colored by the proximity-to-scission index η_i. Coordinates are normalized by the current cell dimensions $(x/L_x, y/L_y)$. (B, F, J) Filtered configurations showing only near-scission strands with $\eta_i > 0.9$. (C, G, K) Probability distributions of η_i in the undeformed state, at an intermediate stretch, and at the stretch of peak stress $\lambda_{\max}$. (D, H, L) Fraction of broken and detangled strands as a function of stretch. Vertical dashed lines indicate $\lambda_{\max}$.

As C decreases, η becomes more uniform across the network (Fig. 6A, E, I). Since force increases monotonically with η, these configurations also provide a qualitative picture of the spatial distribution of forces. The crosslink-dominated network (high-C) contains a broad mixture of weakly stretched and near-scission strands, whereas the entanglement-dominated network (low-C) contains a much larger population of highly stretched strands. This difference is clearer when only highly stretched strands with $\eta_i > 0.9$ are plotted (Fig. 6B, F, J). At $C = 3 \times 10^{-3}$, near-scission strands are relatively sparse and spatially isolated. At $C = 1.2 \times 10^{-3}$, their number and spatial coverage decreases while being more isolated. At $C = 1.2 \times 10^{-5}$, their number and spatial coverage increase, forming multiple percolated pathways that span the network. We further analyze the force distribution by plotting the probability distributions of η (Fig. 6C, G, K). At $C = 3 \times 10^{-3}$, the distribution

at $\lambda = 1$ has a broad peak at low η with a long tail toward larger η. At an intermediate stretch ($\lambda = 2.3$), the distribution spreads across nearly the entire range of η. At the stretch of peak stress ($\lambda_{\max} = 3.6$), the distribution is highly left skewed toward $\eta = 1$, while a substantial population remains at much smaller η. The broad shape indicates highly nonuniform recruitment: some strands are already near scission while many others remain weakly stretched. At $C = 1.2 \times 10^{-3}$, the distribution is more clearly unimodal ($\lambda = 1$), and the peak translates toward larger η as λ increases ($\lambda = 2.4$ and $\lambda_{\max} = 3.9$), showing that a greater fraction of the strands is progressively recruited. At $C = 1.2 \times 10^{-5}$, the entanglement-dominated network exhibits a narrower peak at $\lambda = 1$. As λ increases ($\lambda = 3.2$), the peak translates toward $\eta = 1$, while retaining a comparatively narrow distribution. The distribution at $\lambda_{\max} = 5.4$ becomes left-skewed since it is bounded by the scission condition at $\eta = 1$, but most strands remain concentrated in the high-η range, indicating more uniform strand recruitment.

During deformation, strands can be removed by either strand scission or detanglement (Fig. 6D, H, L). At $C = 3 \times 10^{-3}$, the network damage proceeds only through strand scission since all nodes represent crosslinks. At $C = 1.2 \times 10^{-3}$, the scission and detanglement of strands coexist, and the detanglement accounts for the larger part of the accumulated damage. At $C = 1.2 \times 10^{-5}$, more junctions are entanglements so detanglement becomes a major component of damage. The accumulated damage at $\lambda_{\max}$ (vertical dashed lines) shows a different trend with C. At high C, a substantial amount of damage accumulates before peak stress. By contrast, at low C, a negligible amount of damage is observed before peak stress.

Together, Figs. 5 and 6 demonstrate how strength is governed by C. Increasing C shortens the strands between crosslinks and reduces the relative contribution of entanglements, with little change in modulus but a more heterogeneous load distribution. For crosslink-dominated networks without entanglements, the network can only redistribute load by strand scission, and the percolation of near-scission strands is weak (Fig. 6B). The probability distribution of η at peak stress is broad, showing that most strands are weakly loaded (Fig. 6C). The macroscopic load is therefore concentrated within a small fraction of the network, causing the percolated paths to rupture before recruiting the rest of the network. Decreasing C produces longer strands between crosslinks and accommodates more entanglements. Longer strands provide more extension before scission, and entanglement slippage relaxes highly stretched strands by allowing them to exchange contour length with less stretched neighboring strands, promoting load transfer. Consequently, a larger population of near-scission strands (Fig. 6K) forms multiple percolated paths in the entanglement-dominated network (Fig. 6J). These percolated paths carry load collectively and in parallel, allowing the network to sustain a higher macroscopic stress. The network at intermediate C represents a crossover between these two limiting behaviors. While the probability distribution is narrower than that of high C (Fig. 6G), the network does not show clearly percolating paths (Fig. 6F). The entanglement population remains insufficient to form multiple percolated paths and share loads collectively across the network (Fig. 6J), resulting in a mild change in strength. Furthermore, decreasing C also delays damage initiation (Fig. 6D, H, L) and shifts the damage mechanism from strand scission towards detanglement. Overall, strength is governed by network homogeneity and load redistribution. The low-C network reaches higher strength through the collective loading of a larger strand population, whereas the high-C network exhibits low strength due

to extreme loading of only a small subset. Strength is therefore governed not simply by the number of crosslinks, but by the ability of the network to redistribute load before its near-scission strand population loses connectivity.

4.2. Effect of water-to-monomer molar ratio W

We next vary the water-to-monomer molar ratio W, while holding the other preparation variables C and λ_p. Experimentally, PAAm hydrogels are synthesized with $W = 2$, 8, 15, and 22 at fixed $C = 6 \times 10^{-4}$, and are tested in their as-prepared states. The value of C is chosen to be sufficiently low, such that a wide range of entanglement fractions c_e can be studied with the given values of W. Computationally, the values of W are used to determine the initial polymer fraction ϕ_{init}, the mean number of Kuhn segments per strand $\overline{N}_{\text{K}}$, and c_e. The values of network structural parameters used are listed in Table A.3. Increasing W decreases ϕ_{init}, increases the characteristic entanglement length N_e and $\overline{N}_{\text{K}}$, and reduces c_e. At $W = 22$, N_e exceeds N_c, and the simulated network is treated as unentangled.

The experimental stress–stretch curves show that increasing W decreases the strength while increasing the stretchability (Fig. 7A, C, D). The simulations reproduce both trends (Fig. 7B, C, D). The experimental results show that the work of fracture decreases as W increases, whereas the simulation results do not show a clear trend, which will be discussed later (Fig. 7E). The modulus decreases with increasing W in both experiments and simulations (Fig. 7F).

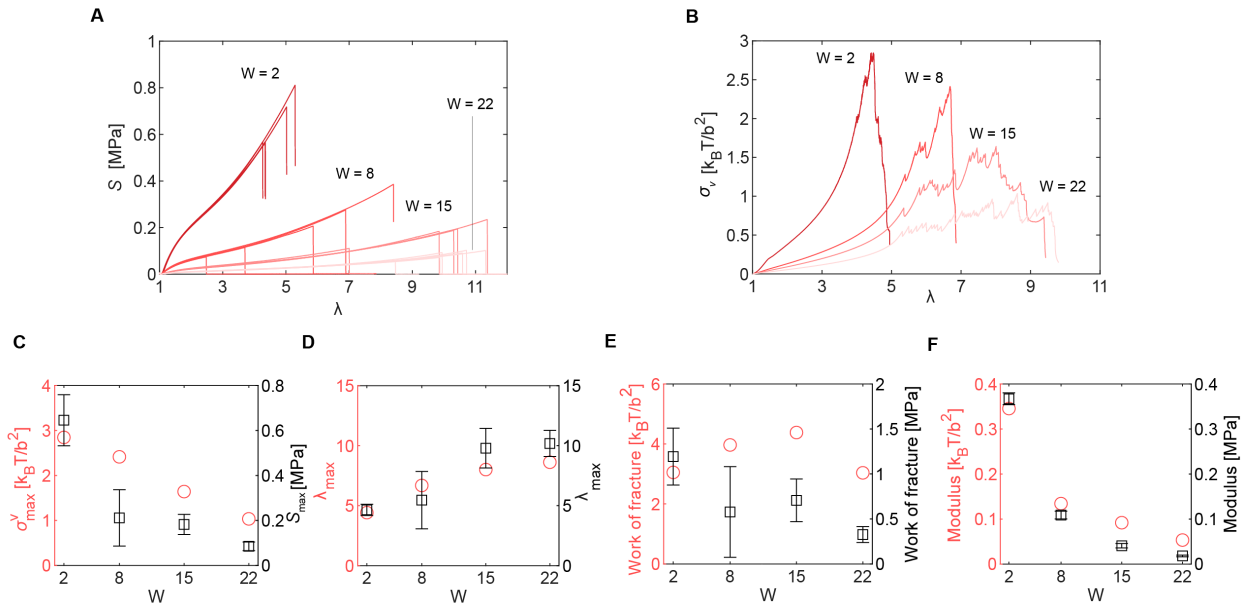


Figure 7: Effect of the water-to-monomer molar ratio W on the stress–stretch curves under uniaxial tension at fixed $C = 6 \times 10^{-4}$ and $\lambda_p = 1$. (A) Experimental nominal stress–stretch curves and (B) simulated nominal virial stress–stretch curves for networks with different W. (C–F) Strength, stretchability λ_{max}, work of fracture and modulus as functions of W. Simulation results are shown in red and referenced to the left axes, whereas experimental measurements are shown in black and referenced to the right axes.

We next investigate the corresponding microscopic responses for $W = 2$ and $W = 15$, while keeping $\lambda_p = 1$ (Fig. 8A–D vs E–H, respectively). The network configurations at

the peak stress show that the $W = 2$ network has more uniform mesh sizes in normalized coordinate, indicating more homogeneous distribution of nodes (Fig. 8A and E). Also, the $W = 2$ network contains a larger fraction of highly stretched strands on average. The filtered configurations are comparable between $W = 2$ and $W = 15$, suggesting that W and the degree of force percolation are weakly correlated (Fig. 8B and F). However, the difference between $W = 2$ and $W = 15$ is noticeable in the probability distribution of η. For $W = 2$, the probability distribution at $\lambda = 1$ is unimodal and centered near $\eta = 0.3$. At intermediate stretch ($\lambda = 2.7$), the peak shifts to $\eta = 0.55$ in a similarly narrow shape. At peak stress ($\lambda_{\max} = 4.4$), the distribution becomes left-skewed and develops a strong accumulation near $\eta = 1$. For $W = 15$, the undeformed distribution at $\lambda = 1$ is shifted toward a smaller η. At intermediate stretch ($\lambda = 4.5$), it broadens across a wide range of η. At peak stress ($\lambda_{\max} = 8.0$), the distribution develops a peak near $\eta = 1$ but is accompanied by a broad tail extending toward low η, indicating that more weakly stretched strands are present at the peak stress than that in $W = 2$.

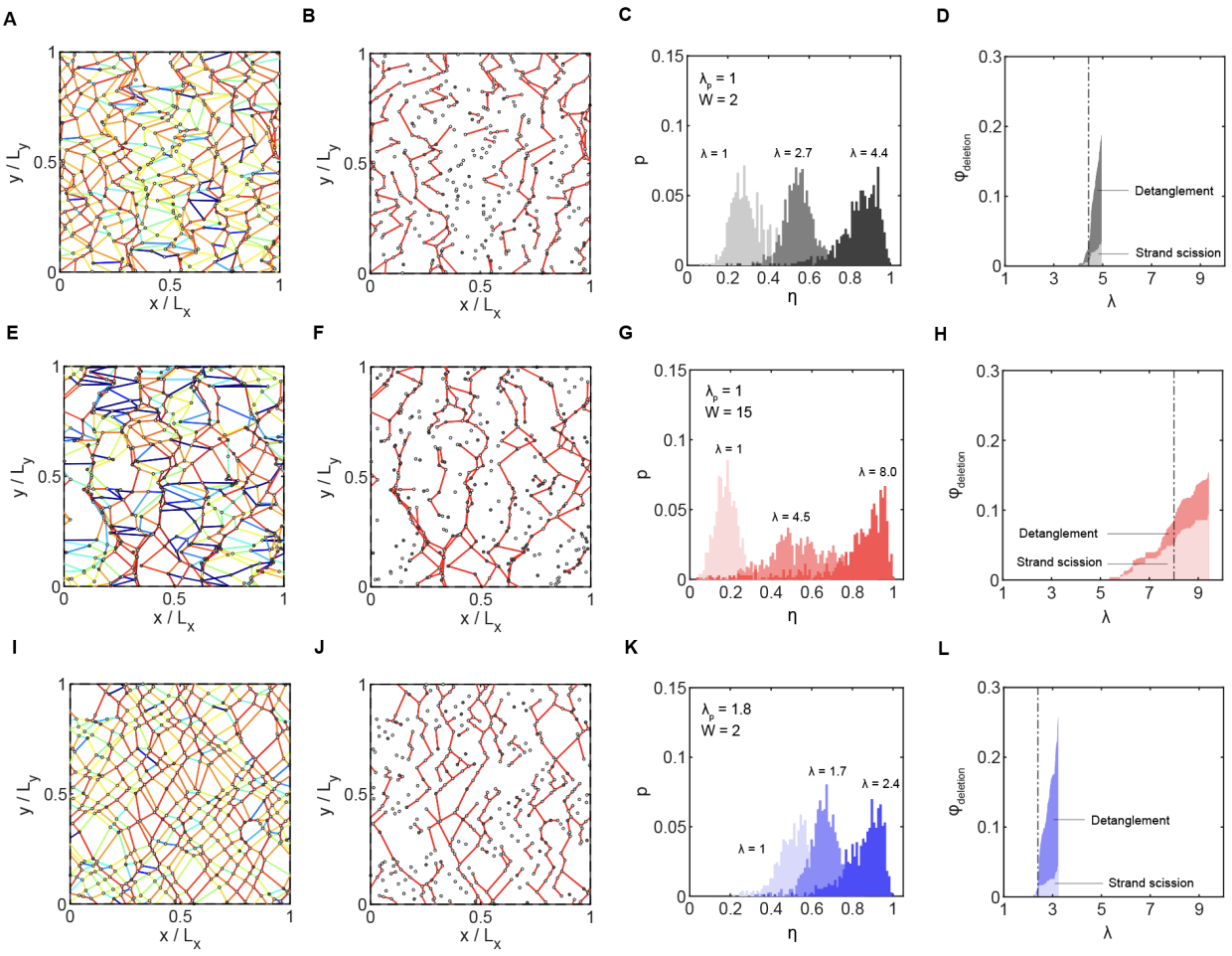


Figure 8: Network configuration and force distribution under independent variations of water-to-monomer molar ratio W and swelling-induced prestretch λ_p at fixed $C = 6\times10^{-4}$: (A–D), (E–H), and (I–L) correspond to $(W, \lambda_p) = (2, 1)$, $(15, 1)$, and $(2, 1.8)$, respectively. (A, E, I) Network configurations at peak stress, colored by the proximity-to-scission index η_i. Coordinates are normalized by the current cell dimensions $(x/L_x, y/L_y)$. (B, F, J) Filtered configurations showing only near-scission strands with $\eta_i > 0.9$. (C, G, K) Probability distributions of η_i in the undeformed state, at an intermediate stretch, and at the stretch of peak stress. (D, H, L) Fractions of broken and detangled strands as functions of stretch. The vertical dashed lines indicate the stretch of peak stress, $\lambda_{\max}$.

The damage histories also change with W(Fig. 8D and H). At $W = 2$, strand scission and detanglement begin near $\lambda = 4$, followed by failure at $\lambda_{\max} = 4.4$. At $W = 15$, both scission and detanglement begin at a larger stretch near $\lambda = 5$ and accumulate progressively over a broader stretch interval before peak stress around $\lambda_{\max} = 8$. Detanglement is the larger contribution for both conditions. The discrete stress drops in the simulated curves (Fig. 7B) coincide with these individual scission and detanglement events.

Together, Figs. 7 and 8 show that increasing W reduces strength through changes in both strand density and strand loading. Higher W lowers the polymer content and produces fewer but longer strands per unit volume. The lower strand density contributes to the reductions in modulus and strength (Fig. 7C and F). The network configuration at higher W exhibits a more heterogeneous spatial distribution of nodes and also a smaller fraction of near-scission

strands, indicating less uniform recruitment of strands (Fig. 8A and E). In addition, increasing W reduces the entanglement fraction, which limits contour-length redistribution among strands. Consequently, the broad probability distribution at the peak stress of a high W contains many strands that are moderately loaded (Fig. 8C and G). The macroscopic load is therefore supported by fewer strands and is distributed less uniformly than that at a lower W, resulting in lower strength. Moreover, longer strands at high W provide greater extensibility, thereby delaying damage initiation with more damage accumulation upon increasing $\lambda_{\max}$ (Fig. 8D and H). The non-monotonic trend in work of fracture (Fig. 7E) reflects these opposing changes in stress scale and extensibility in the model. In the experiments, by contrast, the dilution has a stronger effect on load-bearing strand density than is captured by the idealized two-dimensional network, which can lead to a monotonic decrease of work of fracture with W. Overall, decreasing W increases the strength through increased strand density with entanglements, more uniform spatial distribution of forces, and fewer weakly stretched strands, but sacrifices the stretchability due to shortened strand length.

4.3. Effect of swelling-induced prestretch λ_p

We next vary the swelling-induced prestretch $\lambda_{p,\text{exp}}$ while holding the precursor composition fixed at $W = 2$ and $C = 6 \times 10^{-4}$. Experimentally, the PAAm hydrogels are swollen to obtain $\lambda_{p,\text{exp}} = 1$, 1.36, 1.46, and 1.49, corresponding to $\lambda_p = 1, 1.59, 1.76$, and 1.80. In the simulation, we choose representative values of $\lambda_p = 1$, 1.2, 1.5, and 1.8. The values of network structural parameters used are listed in Table A.4. Recall that swelling is modeled as a two-dimensional isotropic dilation (Eq. (14)). Since swelling occurs after network formation, it does not change the assigned strand contour lengths or the initial network connectivity. Instead, increasing λ_p increases the initial end-to-end distances of the strands and reduces the strand densities.

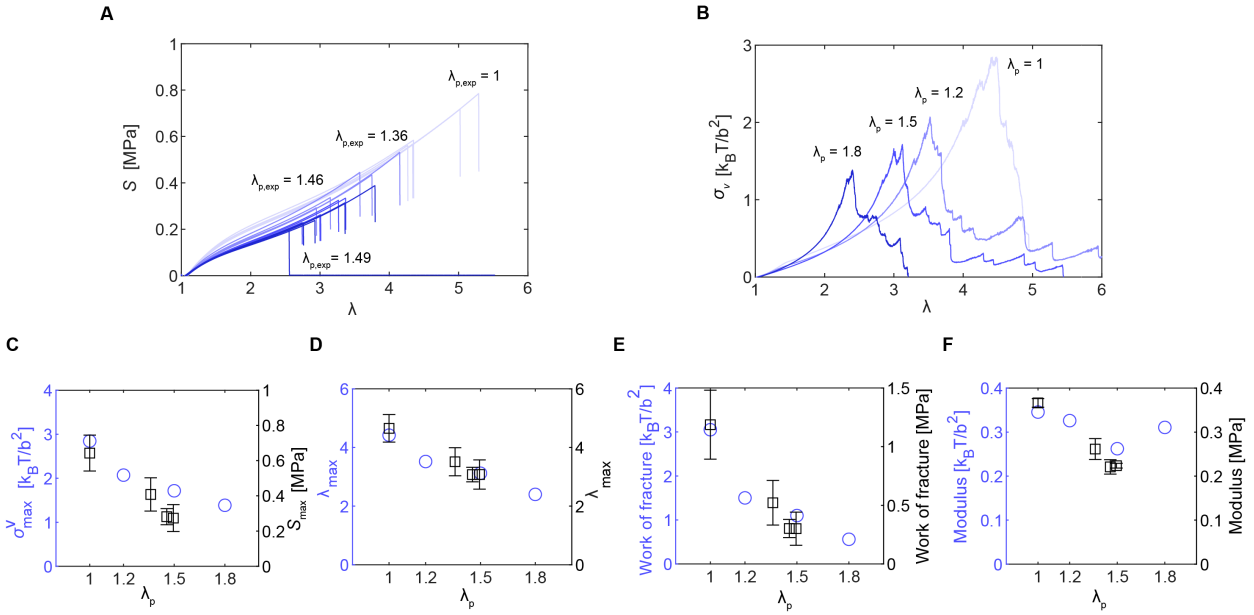


Figure 9: Effect of swelling-induced prestretch λ_p on stress–stretch curves under uniaxial tension at fixed $W = 2$ and $C = 6 \times 10^{-4}$. (A) Experimental nominal stress–stretch curves with different $\lambda_{p,\mathrm{exp}}$ and (B) simulated virial stress–stretch curves for networks with different λ_p. (C–F) Strength, stretchability λ_{max}, work of fracture, and modulus as functions of λ_p. Simulation results are shown in blue and referenced to the left axes, whereas experimental measurements are shown in black and referenced to the right axes.

The experimental stress–stretch curves show that increasing λ_p decreases the strength, stretchability and work of fracture, which align with the trends of simulations (Fig. 9A–E). The experimental modulus decreases monotonically with λ_p, whereas the simulated modulus decreases up to an intermediate λ_p and then increases (Fig. 9F).

We then investigate the microscopic effects of prestretch by comparing $\lambda_p = 1$ and $\lambda_p = 1.8$ at fixed $W = 2$ and $C = 6 \times 10^{-4}$ (Fig. 8A–D and I–L, respectively). Note that the network configuration with normalized coordinates does not directly display the reduction in physical strand density caused by dilation. Similarly, the probability distribution and damage fraction are normalized by the number of strands and therefore describe the behavior of the strand population rather than its density. At peak stress, both networks show similarly distributed populations of highly stretched strands (Fig. 8A and I). The filtered configurations likewise show similarly weak percolation in the loading direction (Fig. 8B and J). Therefore, the two networks reach qualitatively similar configurations at peak stress, although the prestretched network reaches the peak stress at a much smaller stretch (Fig. 8C and K). For the network without dilation $\lambda_p = 1$, the distribution at $\lambda = 1$ has a narrow mode at $\eta = 0.3$. As the network is stretched, this mode translates toward larger η at $\lambda = 2.7$, and the distribution becomes left-skewed with an accumulation near $\eta = 1$ at $\lambda_{\mathrm{max}} = 4.4$. For the network with strong dilation $\lambda_p = 1.8$, the initial distribution already shifts into the intermediate-η range with a mode close to $\eta = 0.6$. The mode moves farther toward $\eta = 1$ at the intermediate stretch ($\lambda = 1.7$), and a high-η population develops at peak stress ($\lambda_{\mathrm{max}} = 2.4$).

The damage histories also differ with λ_p (Fig. 8D and L). For $\lambda_p = 1$, strand scission and detanglement begin near $\lambda = 4$, and the stress reaches the peak near $\lambda_{\mathrm{max}} = 4.4$.

For $\lambda_p = 1.8$, damage initiates near $\lambda = 2$, and the stress reaches the peak near $\lambda_{\max} = 2.4$. Detanglement is the larger contribution in both cases. Increasing prestretch therefore does not introduce a different damage mechanism, but shifts the onset and accumulation of damage to smaller stretches.

Together, Figs. 9 and 8 show that swelling affects the network strength through the combined effects of dilution and strand prestretch. Swelling reduces the number of load-bearing strands per unit area in the two-dimensional model and per unit volume in the experiments, lowering the macroscopic stress scale and thereby lowering modulus. Swelling shifts the initial strand population toward larger η without changing the strand contour lengths, prestretching the strands. The strands therefore have less remaining extensibility and approach scission over a smaller deformation interval. The similar probability distributions at peak stress indicate network configurations with similar load distribution and heterogeneity (Fig. 8C and K); the prestretched network simply reaches this state earlier and with fewer strands per unit area. These effects explain the simultaneous reductions in strength, stretchability, and work of fracture, as well as the earlier onset of scission and detanglement. The modulus reflects two opposing contributions: dilution reduces the strand density, whereas prestretch increases the tangent stiffness of each strand by moving it into a steeper region of its nonlinear force–extension relation. At large λ_p, the experimental modulus keeps decreasing but the simulation modulus increases, which we attribute to the weaker dilution effects in two-dimensional dilution than volumetric dilution. Overall, we show that strength can be governed by the coupled effect of dilution and strand prestretch due to swelling, rather than the spatial or statistical distribution of forces across the network.

4.4. Coupled effects of polymer content and prestretch

We next vary the water-to-monomer molar ratio W and the swelling-induced prestretch $\lambda_{p,\mathrm{exp}}$ simultaneously while fixing $C = 6 \times 10^{-4}$. Experimentally, a previous study prepared PAAm hydrogels with $W = 2$, 8, 15, or 22 and then swelled the hydrogels to the polymer content of the as-prepared $W = 22$ network, and reported the mechanical properties [7]. The final polymer content is therefore approximately the same for all specimens. Computationally, the corresponding coupled series are $(W, \lambda_p) = (2, 2.1)$, $(8, 1.5)$, $(15, 1.2)$, and $(22, 1)$. These λ_p values are chosen such that the final polymer content satisfies $\phi = \phi_{\mathrm{init}}(W)/\lambda_p^2 \approx$ constant. Increasing W independently decreases ϕ_{init}, increases $\overline{N}_{\mathrm{K}}$, and reduces c_e, while the constraint of final polymer content results in decreasing λ_p. The values of network structural parameters used are listed in Table A.5.

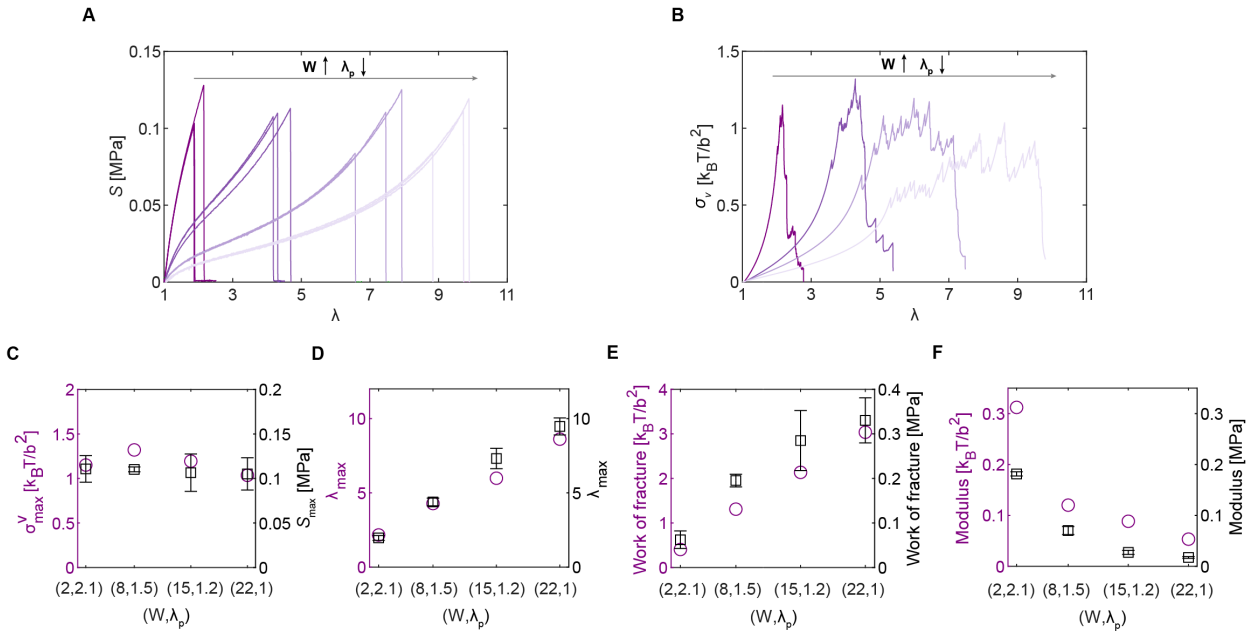


Figure 10: Coupled effects of the water-to-monomer molar ratio W and swelling-induced prestretch λ_p on the stress–stretch curves under uniaxial tension at fixed $C = 6 \times 10^{-4}$ and approximately constant final polymer content. (A) Experimental nominal stress–stretch curves [7] and (B) simulated virial stress–stretch curves for $(W, \lambda_p) = (2, 2.1)$, $(8, 1.5)$, $(15, 1.2)$, and $(22, 1)$. (C–F) Strength, stretchability $\lambda_{\max}$, work of fracture, and modulus across the series of (W, λ_p). Purple circles denote simulation results referenced to the left axes, whereas black squares denote experimental measurements referenced to the right axes.

The experimental stress–stretch curves show that (W, λ_p) with higher W and lower λ_p exhibits higher stretchability without changing strength (Fig. 10A). The simulations reproduce both trends (Fig. 10B). The strength remains almost constant across the coupled series in both the experiments and simulations (Fig. 10C). By contrast, stretchability and work of fracture increase strongly from $(W, \lambda_p) = (2, 2.1)$ to $(22, 1)$ (Fig. 10D and E). The modulus follows the opposite trend (Fig. 10F).

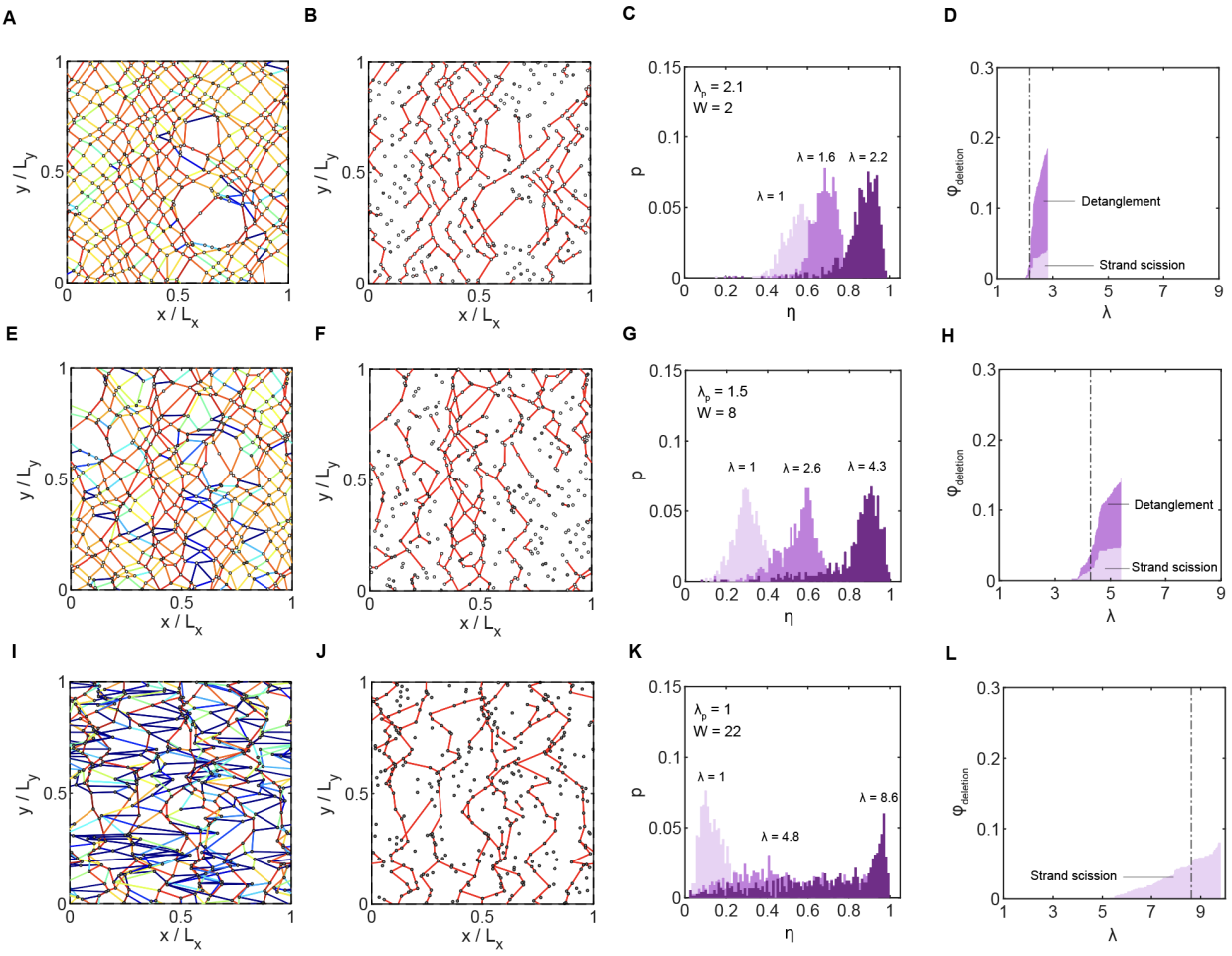


Figure 11: Network configuration and force distribution under coupled variations of the water-to-monomer molar ratio W and swelling-induced prestretch λ_p at fixed $C = 6 \times 10^{-4}$ and approximately constant final polymer content: (A–D), (E–H), and (I–L) correspond to $(W, \lambda_p) = (2, 2.1)$, $(8, 1.5)$, and $(22, 1)$, respectively. (A, E, I) Network configurations at peak stress, colored by the proximity-to-scission index η_i. Coordinates are normalized by the current cell dimensions $(x/L_x, y/L_y)$. (B, F, J) Filtered configurations showing only near-scission strands with $\eta_i > 0.9$. (C, G, K) Probability distributions of η in the undeformed state, at an intermediate stretch, and at the stretch of peak stress. (D, H, L) Fractions of broken and detangled strands as functions of applied stretch. Vertical dashed lines indicate the stretch of peak stress, $\lambda_{\max}$.

The corresponding microscopic responses are shown for three representative coupled series (Fig. 11A–D, E–H, and I–L with $(W, \lambda_p) = (2, 2.1), (8, 1.5)$, and $(22, 1)$, respectively). The coupled series span from a network formed at high polymer content and subsequently subjected to large swelling to a network formed directly at the final polymer content without swelling. At $(W, \lambda_p) = (2, 2.1)$, a large portion of the network is highly stretched (Fig. 11A). At $(W, \lambda_p) = (8, 1.5)$, the network contains a broader mixture of strand extensions (Fig. 11E). The network of $(W, \lambda_p) = (22, 1)$ exhibits the greatest visual variation in η, with a smaller population of near-scission strands (Fig. 11I). The filtered configurations show no significant difference in percolation (Fig. 11B, F and J). The probability distributions show that the initial strand population shifts progressively towards low η from $(W, \lambda_p) = (2, 2.1)$ to $(22, 1)$ (Fig. 11C, G, and K). For $(W, \lambda_p) = (2, 2.1)$, the initial distribution at $\lambda = 1$ is centered

near $\eta = 0.6$. The peak translates toward $\eta = 1$ over a relatively small stretch interval while retaining a narrow shape ($\lambda = 1.6, \lambda_{\max} = 2.2$). For $(W, \lambda_p) = (8, 1.5)$, the peak at $\lambda = 1$ is located near $\eta = 0.3$ and translates progressively toward $\eta = 1$ as the stretch increases ($\lambda = 2.6, \lambda_{\max} = 4.3$). For $(W, \lambda_p) = (22, 1)$, the initial distribution at $\lambda = 1$ is concentrated near $\eta = 0.1$. At the intermediate stretch ($\lambda = 4.8$), it broadens across nearly the full range of η. At the peak stress ($\lambda_{\max} = 8.6$), a terminal accumulation develops near $\eta = 1$, accompanied by a broad population of less stretched strands. The coupled change from $(W, \lambda_p) = (2, 2.1)$ to $(22, 1)$ therefore shifts the initial population towards less stretched states and forms a less uniform distribution at peak stress.

The damage histories show a corresponding delay in microscopic damage (Fig. 11D, H, and L). For $(W, \lambda_p) = (2, 2.1)$, strand scission and detanglement begin at a small applied stretch and accumulate rapidly over a narrow deformation interval. At $(W, \lambda_p) = (8, 1.5)$, both processes begin later and accumulate over a broader interval, with detanglement remaining the larger contribution. For $(W, \lambda_p) = (22, 1)$, the network is unentangled; therefore the damage proceeds entirely through strand scission. The strand scission begins at a substantially larger stretch and accumulates gradually through the peak-stress configuration.

Together, Figs. 10 and 11 demonstrate how networks with different preparation variables but the same final polymer content can reach similar strengths through different microscopic load-bearing states. At low W and high λ_p, the network forms with more entanglements and shorter strands. Subsequent swelling strongly prestretches these strands, producing a dense population of near-scission strands (Fig. 11C). The greater entanglement density and strand prestretch result in a larger modulus, but the limited remaining extensibility after swelling causes damage to begin early. At high W and low λ_p, the network forms with fewer entanglements and longer strands, and undergoes less prestretch induced by swelling. Its initial strand population is therefore farther from scission, allowing substantially more deformation. Although the probability distribution at peak stress is less uniform (Fig. 11K), the longer and less-prestretched strands retain sufficient extensibility and preserve the degree of percolation (Fig. 11J). Meanwhile, the larger extensibility increases the work of fracture, and the reduction in entanglement density changes the damage mechanism from detanglement to strand scission. Thus, similar strengths across the coupled series do not imply similar microscopic states: the preparation history determines how many load-bearing strands support the network, how rapidly they approach scission, and how the network ultimately loses connectivity.

4.5. General statistical descriptors

The preceding results show that the preparation variables C, W, and λ_p affect structural variables, including strand density, strand length, entanglement fraction, and prestretch, through network configuration and probability distribution, and eventually determine strength. However, the previous subsections investigate the effects of each variable on strength independently, and the coupled series does not alter the strength, limiting understanding of a general microscopic origin of strength. In this subsection, we investigate whether there are general statistical descriptors that are correlated with strength across all preparation variables considered in this study.

We compare the simulated strength $\sigma^v_{\max}$ with six candidate descriptors (Fig. 12). We first examine initial strand density ν_{strand}, which is, overall, strongly associated with strength

since more strands are available to transmit load (Fig. 12A). The data do not, however, collapse onto a common relationship for every preparation variable. In particular, changing C modifies the network topology by changing the ratio between crosslinks and entanglements, in addition to strand density, where the resulting networks exhibit different strengths despite similar strand densities. Although strand density indicates the potential load-bearing population, it does not represent how effectively that population is recruited. The orientation parameter $\langle \cos^2 \theta \rangle$ (Eq. (21)) also shows a generally positive association with strength (Fig. 12B). Nevertheless, networks with values of $\langle \cos^2 \theta \rangle$ close to unity span a wide range of strengths. Alignment along the loading direction indicates that strands are geometrically oriented to transmit the load, contributing to strength. However, it does not specify how many strands carry substantial force nor how uniformly the network shares that load. The stronger networks generally accumulate little damage before peak stress, indicated with the damage index ϕ_{deletion}, whereas weaker networks tend to exhibit greater strand scission or detanglement (Fig. 12C). However, similar values of ϕ_{deletion} can correspond to different strengths, since the distribution of the damage and the connectivity of the surviving network also differ across different network designs.

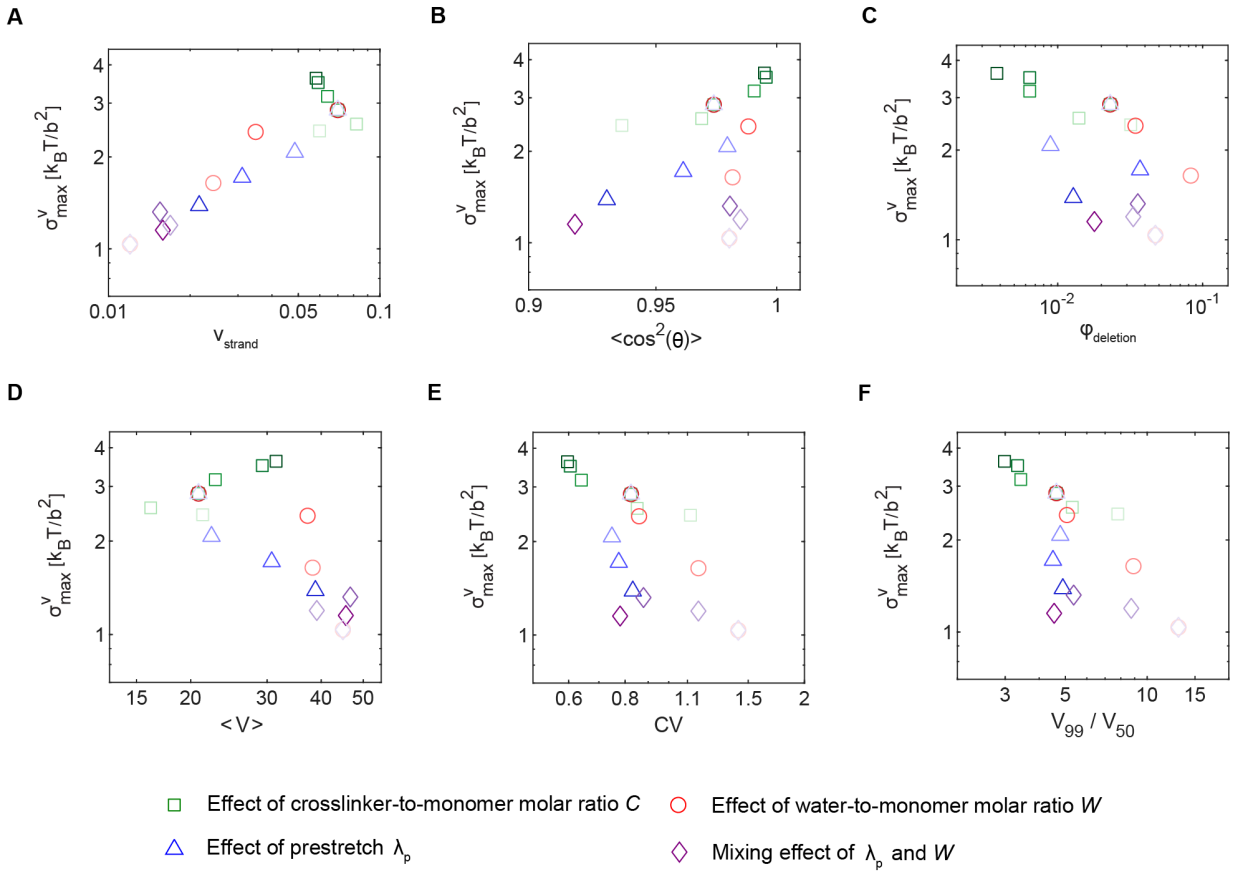


Figure 12: Relationships between simulated strength $\sigma^v_{\max}$ and statistical network descriptors. (A) Initial strand density ν_{strand}. (B) Strand-orientation parameter $\langle \cos^2 \theta \rangle$ at peak stress. (C) Accumulated damage index ϕ_{deletion} at peak stress. (D) Mean virial stress $\langle V \rangle$ at peak stress. (E) Coefficient of variation CV_V at peak stress. (F) Upper-tail heterogeneity ratio V_{99}/V_{50} at peak stress. Here, V_{99} and V_{50} are the 99th-percentile and median virial stresses, respectively. Green squares, red circles, blue triangles, and purple diamonds denote variations in C, W, λ_p and the coupled (W, λ_p) series, respectively. The color gradient from dark to light correspondingly denotes increasing C, increasing W, decreasing λ_p, and increasing W while decreasing λ_p at the same time.

To capture the details of load distribution across different network designs, we consider virial stresses at the strand level V_i to identify more general descriptors. The macroscopic virial stress is the sum of V_i over all active strands, as defined by Eq. (18). Consequently, V_i provides a direct decomposition of the macroscopic tensile stress into the contributions carried by individual strands. Unlike strand extension or force alone, V_i incorporates the tensile force, orientation, and extension of each strand. The statistical distribution of V_i therefore will inform us how the macroscopic stress is distributed globally and locally. The complete distributions of normalized V_i are provided in Appendix B. The shapes of those distributions vary substantially with C, W, and the coupled (W, λ_p) conditions, but change little with λ_p alone. We next analyze strength in terms of the magnitude and heterogeneity of the stress distribution V_i (Fig. 12D–F). The mean virial stress $\langle V \rangle$ does not exhibit a common monotonic relationship with strength (Fig. 12D). Because σ^v is the sum of the strand-level contributions, a large $\langle V \rangle$ can arise when many strands are effectively recruited.

However, it can also arise when the same macroscopic load is concentrated within a smaller surviving population. The mean must therefore be interpreted together with the number of load-bearing strands and the variation among their individual contributions. The coefficient of variation CV_V measures the stress variation among strands relative to the mean. Strength generally decreases as CV_V increases, although scatter remains among different preparation variables (Fig. 12E). This inverse correlation indicates that networks with more uniform load distribution tend to sustain greater macroscopic stress. Note that CV_V measures the dispersity of the distribution around the mean but it does not distinguish whether the distribution is skewed more towards the lower tail or upper tail. The ratio V_{99}/V_{50} more directly characterizes load concentration in the upper tail (Fig. 12F). Here, V_{99} is the stress below which 99% of the strands fall, while V_{50} is the median. A large V_{99}/V_{50} indicates that a small upper-tail population carries substantial load, while the majority of strands in the network do not, resulting in low strength.

Overall, these results identify two general statistical descriptors for strength. The initial strand density ν_{strand} determines the population available to establish load-bearing paths, and the ratio V_{99}/V_{50} characterizes how uniform the load distribution is among highly stretched strands at peak stress. The preparation variables C, W, and λ_p affect both descriptors through different structural variables. The strength is expected to be a collective property of multiple statistical descriptors rather than a function of a single network variable. Strong networks combine a sufficient population of connected strands with relatively uniform load sharing, allowing multiple load-bearing paths to approach their limiting extension simultaneously. Weak networks either contain too few load-bearing strands or concentrate the macroscopic load within a small upper-tail population that fails before the remaining network is fully recruited. Neither ν_{strand} nor V_{99}/V_{50} alone constitutes a material law for strength. Together, however, they provide complementary measures of the available load-bearing population and how effectively a given network distributes load before failure.

5. Conclusions

Although strength has commonly been used to characterize fracture of polymer networks, its microscopic origin has long remained elusive. To systematically investigate how strength is determined, we design both experiments and simulations around a common set of structural variables, compare their results to establish agreement in strength trends, and relate the strength to microscopic load distribution. Experimentally, we choose three representative preparation variables: crosslinker-to-monomer molar ratio, water-to-monomer molar ratio, and prestretch by swelling after synthesis, to modify network structure such as crosslinks, entanglements, and strand length. Computationally, we develop a two-dimensional network model that explicitly distinguishes crosslinks from entanglements and accounts for strand-length polydispersity, nonlinear chain elasticity, strand scission, and detanglement. Although the experimental and simulated stresses have different scales, the model well reproduces the experimental trends in strength. The simulations further provide detailed information on load distribution among strands and damage evolution throughout the network, allowing us to identify statistical descriptors correlated with strength across different network designs.

At fixed polymer content, decreasing the crosslinker-to-monomer molar ratio C changes the network from a crosslink-dominated topology with short strands to an entanglement-

dominated topology with longer strands. The longer strands provide greater extensibility, while entanglements slip and redistribute contour length with load transfer among neighboring strands. These effects promote the formation of load-bearing paths throughout the network, increase strength and stretchability, and delay microscopic damage. Decreasing the water-to-monomer molar ratio W in the as-prepared state increases the initial strand densities, shortens strands, and increases the entanglement fraction. The networks with low W are less stretchable but stiffer and stronger. Increasing the swelling-induced pre-stretch λ_p at fixed precursor composition dilutes the network and reduces the remaining strand extensibility. Consequently, strength and stretchability decrease with earlier damage initiation. The coupled series (W, λ_p) demonstrates that increasing W while decreasing λ_p with a constant polymer content results in networks with similar strengths but substantially different load distributions and damage mechanisms. Similar macroscopic strengths therefore do not imply similar microscopic load-bearing states. Across all preparation variables, we find that strong networks require a sufficient density of connected strands to establish multiple load-bearing paths while preventing the macroscopic load from being concentrated within few near-scission strands. Initial strand density ν_{strand} characterizes the available load-bearing population, and the upper-tail ratio V_{99}/V_{50} characterizes the heterogeneity of load distribution. Neither quantity alone provides a universal law for strength.

The present framework focuses on specific structural features such as crosslinks and entanglements. Other potentially important factors governing strength remain less explored. For example, although the two-dimensional model captures the principal experimental trends, its dimensional reduction limits quantitative comparisons with three-dimensional networks, particularly when swelling changes both strand density and conformation. The model also excludes initial loops and dangling ends. Extending the model to three dimensions and incorporating network defects would allow us to test whether the identified statistical descriptors remain applicable across a broader range of network structures. The present study also does not establish how strength depends on loading rate. The mechanical equilibration procedure does not fully capture the competing timescales of strand relaxation, entanglement sliding, and strand scission. Incorporating the kinetics of these processes and comparing simulations with experiments at different loading rates would clarify how loading conditions affect load redistribution and damage. Initial chain conformation provides another direction for extending the framework. We assume Gaussian statistics for initial strand conformations across this study. Networks prepared with expanded or contracted chain conformations would allow us to examine how the initial chain conformation affects the formation of load-bearing paths and their approach to scission. Introducing cracks would further connect strand-level damage with crack propagation and fracture energy. Despite these limitations, the present results establish a mechanics-based principle for designing stronger polymer networks by jointly controlling strand density and load concentration.

6. Acknowledgment

This work was primarily supported by the National Science Foundation's MRSEC program (DMR-2308691) at the Materials Research Center of Northwestern University. This work was also supported by start-up funds from Northwestern University, the National Science Foundation under CAREER Grant (CMMI-2540898), and the computational resources

provided by Northwestern University's Quest high-performance computing facility.

Appendix A. Numerical implementation

This appendix reports implementation details needed to reproduce the model without repeating the physical definitions and constitutive equations in Section 3.

Appendix A.1. Entanglement slippage, scission, and free-end slipout

For each entanglement connecting the pair of neighboring strands (i, j), we evaluate a local driving measure $\Delta\sigma_{ij}$ due to stress imbalance across the entanglement, where $\Delta\sigma_{ij} > 0$ indicates that strand i is more highly loaded than strand j. Slippage is treated as a thermally activated process with a rate according to the Eyring kinetic theory,

$$k_{\mathrm{sl},ij} = k_0 \exp\left[-\frac{\Delta G - \beta\Delta\sigma_{ij}}{k_{\mathrm{B}}T}\right], \tag{A.1}$$

where k_0 is an attempt slippage frequency, ΔG is the activation barrier for slippage, and $\beta = b^3$ quantifies the volume of a Kuhn segment ($\beta = b^2$ for two-dimensional approximation). Within a numerical timestep Δt, the probability that a slip event occurs for pair (i, j) is given by the Poisson process

$$p_{ij} = 1 - \exp(-k_{\mathrm{sl},ij}\Delta t). \tag{A.2}$$

An event is accepted when a uniform random number $\xi_{ij} \in [0, 1)$ satisfies $\xi_{ij} < p_{ij}$. The recipient gains one Kuhn segment and the donor loses one:

$$N_{\mathrm{K},i} \leftarrow N_{\mathrm{K},i} + 1, \qquad N_{\mathrm{K},j} \leftarrow N_{\mathrm{K},j} - 1. \tag{A.3}$$

The corresponding update is applied along both primitive paths as shown in Fig. 2B. This update conserves contour length locally,

$$N_{\mathrm{K},i} + N_{\mathrm{K},j} = \mathrm{const.} \tag{A.4}$$

After a strand i reaches $\eta_i = 1$, it is deleted from the active connectivity and its contour is equally divided between two dangling ends q and s:

$$N_{\mathrm{K},i}^{(q)} = N_{\mathrm{K},i}^{(s)} = \frac{1}{2}N_{\mathrm{K},i}. \tag{A.5}$$

These dangling ends do not carry load across the network. If a dangling end is adjacent to an entanglement, accepted slip events transfer contour from the dangling side toward the loaded side until the free end slips through the constraint. The entanglement is then deleted or the free end is advanced to the next constraint along the primitive path, as dictated by the remaining topology.

Within one loading increment, the numerical sequence is: (i) apply the affine cell deformation; (ii) relax nodal positions; (iii) evaluate and accept slippage events; (iv) re-equilibrate after any contour transfer; (v) delete all strands satisfying the scission criterion; (vi) create and update dangling ends and remove exhausted entanglements; and (vii) re-equilibrate before recording stress.

Appendix A.2. Network generation and periodic kinematics

The cell contains $\mathcal{N}$ nodes initialized on a rhombic lattice. Candidate connections are identified within a cutoff distance r_{cut}, and the functionality of each node is set to four. Strands may cross the boundaries of the primary cell, so the topology remains continuous under periodic replication. A fraction c_e of junctions is selected at random among all junctions, and designated as slip-active entanglements; the remaining junctions are crosslinks. The length of each strand is assigned in terms of Kuhn segments through an independent draw from Eq. (8).

For a periodic cell of dimensions $L_x \times L_y$, a nodal coordinate (x_i,y_i) is wrapped into the primary image according to

$$x_i \leftarrow x_i - L_x \,\mathrm{round}\left(\frac{x_i - c_x}{L_x}\right), \qquad y_i \leftarrow y_i - L_y \,\mathrm{round}\left(\frac{y_i - c_y}{L_y}\right), \tag{A.6}$$

where $\mathbf{c}$ is the cell center. The minimum-image convention is used for strands crossing a periodic boundary, where pair-separation vectors are evaluated similarly:

$$\begin{aligned} \Delta x_{ij} &\leftarrow \Delta x_{ij} - L_x \,\mathrm{round}\left(\frac{\Delta x_{ij}}{L_x}\right), \\ \Delta y_{ij} &\leftarrow \Delta y_{ij} - L_y \,\mathrm{round}\left(\frac{\Delta y_{ij}}{L_y}\right). \end{aligned} \tag{A.7}$$

These operations are applied after every affine update and every relaxation iteration. No Dirichlet, traction, or free-surface boundary nodes are used.

Appendix A.3. Mechanical equilibration

The initial assignment of strand lengths, as well as subsequent swelling, deformation, slippage, and damage, generally produces nonzero net forces on the nodes. Mechanical equilibrium is obtained by iteratively updating the position of each node using

$$\mathbf{x}_{k+1}^{\alpha} = \mathbf{x}_k^{\alpha} + \frac{\Delta t}{\zeta}\mathbf{f}_k^{\alpha}, \tag{A.8}$$

where k denotes the relaxation iteration, $\mathbf{x}_k^{\alpha}$ and $\mathbf{f}_k^{\alpha}$ are the position and net force of node α at iteration k, respectively, Δt is the numerical time step, and ζ is the nodal friction coefficient. $\Delta t/\zeta$ is a numerical damping coefficient, which controls the displacement produced by a given force. Iteration continues until the average magnitude of the nodal residual forces satisfies

$$\frac{1}{\mathcal{N}}\sum_{\alpha=1}^{\mathcal{N}} \|\mathbf{f}^{\alpha}\| \le \varepsilon_f, \tag{A.9}$$

where $\mathcal{N}$ is the number of nodes included in the calculation and ε_f is the prescribed force tolerance.

Loading is applied incrementally, with n denoting the index of loading step, distinct from the relaxation-iteration index k. Let $\mathbf{F}_n$ and $\mathbf{F}_{n+1}$ denote the imposed deformation gradients relative to the reference configuration at successive loading steps. The incremental deformation gradient is

$$\Delta\mathbf{F}_n = \mathbf{F}_{n+1}\mathbf{F}_n^{-1}. \tag{A.10}$$

For the area-preserving loading path, $\det(\Delta\mathbf{F}_n) = 1$. The periodic cell and nodal coordinates are first deformed affinely about the cell center, which remains fixed during the increment. For node α,

$$\mathbf{x}_{\text{aff}}^{\alpha,n+1} = \mathbf{c}^n + \Delta\mathbf{F}_n \left(\mathbf{x}^{\alpha,n} - \mathbf{c}^n\right), \tag{A.11}$$

where $\mathbf{x}^{\alpha,n}$ is the relaxed nodal position at loading step n, $\mathbf{c}^n$ is the cell center, and $\mathbf{x}_{\text{aff}}^{\alpha,n+1}$ is the position immediately after the affine update. The deformed cell dimensions are then held fixed while the nodes relax according to Eq. (A.8). These additional displacements allow the local deformation to depart from the imposed affine deformation. After each relaxation update, nodes that cross a periodic boundary are mapped back into the primary cell using the periodic boundary conditions in Appendix A.2.

Appendix A.4. Model parameters and convergence

Appendix A.4.1. Fixed parameters

The fixed parameters already established in the manuscript are summarized below.

Table A.1: Fixed model parameters and numerical controls.

Quantity	Symbol	Value
Number of RVE nodes	$\mathcal{N}$	400
Junction functionality	z	4
Monomers per Kuhn segment	n_{K}	10
Reference entanglement length	N_e^0	10 Kuhn segments
Schulz–Zimm shape parameter	α	2
Polydispersity index	PDI	1.5
Chain-conformation exponent	ν	1/2
Repulsion exponent	γ	2
Scission proximity	$r/(N_{\text{K}}b)$	0.98
Kuhn length	b	1
Thermal energy	$k_{\text{B}}T$	1
Repulsion energy and cutoff range	ϵ, R_c	$1.3\,k_{\text{B}}T, \sqrt{2}r_0$
Connectivity cutoff	r_{cut}	$1.1r_0$
Attempt rate	k_0	$10^6\,t^{-1}$
Activation barrier and bias	$\Delta G, \beta$	$10k_{\text{B}}T, b^2$
Numerical timestep	Δt	$0.05\,t$
True strain rate and incremental stretch ratio	$\dot{\varepsilon}_{yy}, \lambda_{n+1}/\lambda_n$	$0.01\,t^{-1}, 1.0005$
Friction coefficient and numerical dampling coeffcient	$\zeta, \Delta t/\zeta$	$50, 1.0 \times 10^{-3}$
Mean residual-force tolerance	ε_f	0.01
Independent realizations	N_{indep}	3

Finite-size convergence was assessed using networks containing $\mathcal{N} = 169$, 225, 400, 625, 900, and 1225 nodes. Increasing the system size beyond $\mathcal{N} = 400$ produced no appreciable change in the mechanical response, supporting the use of $\mathcal{N} = 400$ throughout this study. We use reduced units in which $k_{\text{B}}T = 1$ and $b = 1$, so the characteristic force scale $k_{\text{B}}T/b$ is also unity.

Appendix A.4.2. Network structural parameters

The network structural parameters used in the four preparation series are summarized in Tables A.2–A.5. Here, c_e is the fraction of entanglement junctions, N_e is the concentration-dependent entanglement length used in the mapping, N_c is the mean number of Kuhn segments between chemical crosslinks, and $\overline{N}_{\mathrm{K}}$ is the mean number of Kuhn segments per strand. All strand and entanglement lengths are expressed as numbers of Kuhn segments. Cases with $c_e = 0$ are treated as unentangled networks.

Table A.2: Network structural parameters for variation of C at fixed $W = 2$ and $\lambda_p = 1$.

C	c_e	N_e	N_c	$\overline{N}_{\mathrm{K}}$
1.2×10^{-5}	0.99	17.3	4167	17.2
6×10^{-5}	0.98	17.3	833	16.9
3×10^{-4}	0.91	17.3	167	15.6
6×10^{-4}	0.83	17.3	83	14.3
1.2×10^{-3}	0.71	17.3	42	12.2
3×10^{-3}	0	17.3	16.7	16.7

Table A.3: Network structural parameters for variation of W at fixed $C = 6 \times 10^{-4}$ and $\lambda_p = 1$.

W	c_e	N_e	N_c	$\overline{N}_{\mathrm{K}}$
2	0.83	17	83	14
8	0.66	44	83	29
15	0.51	81	83	41
22	0	125	83	83

Table A.4: Network structural parameters for variation of swelling-induced prestretch λ_p at fixed $W = 2$ and $C = 6 \times 10^{-4}$.

W	λ_p	c_e	N_e	N_c	$\overline{N}_{\mathrm{K}}$
2	1.0	0.83	17	83	14
2	1.2	0.83	17	83	14
2	1.5	0.83	17	83	14
2	1.8	0.83	17	83	14

Table A.5: Network structural parameters for coupled variation of W and λ_p at fixed $C = 6 \times 10^{-4}$.

W	λ_p	c_e	N_e	N_c	$\overline{N}_{\mathrm{K}}$
2	2.1	0.83	17	83	14
8	1.5	0.66	44	83	29
15	1.2	0.51	81	83	41
22	1.0	0	125	83	83

Appendix B. Probability distributions of virial stress

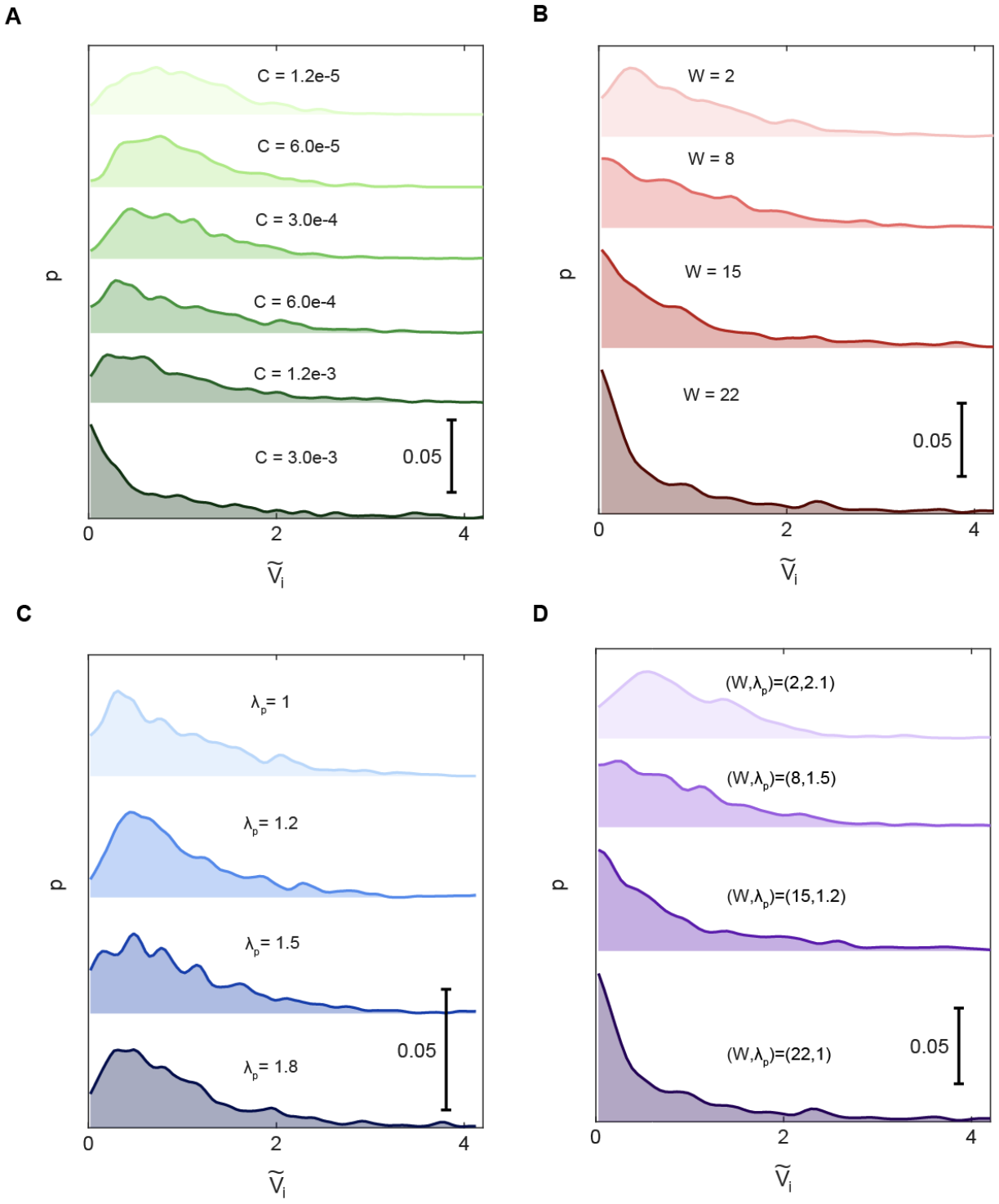


Figure B.13: Probability distributions of the normalized strand-level virial contribution $\widetilde{V}_i$ at the peak-stress configuration. (A) Effect of crosslinker-to-monomer molar ratio C. (B) Effect of water-to-monomer molar ratio W. (C) Effect of swelling-induced prestretch λ_p. (D) Coupled variation of W and λ_p. The distributions are vertically offset for clarity; the vertical scale bar indicates a probability difference of 0.05.

We examine the virial stresses $\widetilde{V}_i$ (Eq. (24)) across the networks at failure, by plotting the probability distribution of $\widetilde{V}_i$ for different preparation variables (Fig. B.13). Note that $\widetilde{V}_i$ is a normalized variable by its mean, allowing us to compare the shape of the virial stress distributions among networks with different macroscopic stress scales. As C decreases, the distribution changes from a sharply decaying curve concentrated near $\widetilde{V}_i = 0$ to a distribution with the peak shifting towards high $\widetilde{V}_i$ (Fig. B.13A). Therefore, the stronger low-C networks contain a larger fraction of strands that contribute significantly to the macroscopic stress. Increasing W produces the opposite change (Fig. B.13B). As W increases, the mode shifts toward zero, the weakly loaded population grows, and the upper tail contracts. This change accompanies the reduction in strength because the network is formed at lower polymer content with fewer entanglements. In contrast, the distributions change little in shape when λ_p is varied independently (Fig. B.13C). Although strength decreases with increasing prestretch, the relative partitioning of load among the strands at peak stress remains similar. The prestretched networks therefore exhibit similar strand-level distributions at peak stress while sustaining different macroscopic stresses. The coupled series provides a complementary result (Fig. B.13D). As W increases and λ_p decreases, the mode shifts toward $\widetilde{V}_i = 0$, even though the networks have approximately the same final polymer content and similar strengths. Therefore, strength is not uniquely determined by the shape of the normalized strand-level distribution. Instead, similar strength can result from different combinations of strand density, strand length, prestretch, and load distribution.

References

[1] H. M. James, E. Guth, Theory of the elastic properties of rubber, The Journal of Chemical Physics 11 (10) (1943) 455–481. doi:10.1063/1.1723785.

[2] E. M. Arruda, M. C. Boyce, A three-dimensional constitutive model for the large stretch behavior of rubber elastic materials, Journal of the Mechanics and Physics of Solids 41 (2) (1993) 389–412. doi:10.1016/0022-5096(93)90013-6.

[3] M. Rubinstein, S. Panyukov, Elasticity of polymer networks, Macromolecules 35 (17) (2002) 6670–6686. doi:10.1021/ma0203849.

[4] G. J. Lake, A. G. Thomas, The strength of highly elastic materials, Proceedings of the Royal Society of London. Series A. Mathematical and Physical Sciences 300 (1460) (1967) 108–119. doi:10.1098/rspa.1967.0160.

[5] T. Kang, J. Dai, Y. Huang, H. Kim, S. Keten, J. Kim, Entanglements and fracture in polymers, Chemical Reviews 125 (22) (2025) 11032–11057.

[6] B. Deng, C. M. Hartquist, S. Wang, X. Zhao, Nonlocal intrinsic fracture energy of polymerlike networks, Physical Review Letters 131 (2023) 228102. doi:10.1103/PhysRevLett.131.228102.

[7] Y. Wang, G. Nian, J. Kim, Z. Suo, Polyacrylamide hydrogels. vi. synthesis-property relation, Journal of the Mechanics and Physics of Solids 170 (2023) 105099.

[8] T. Smith, C. Gupta, Z. Fan, G. J. Brust, R. Vogelsong, C. Carr, S.-Q. Wang, Toughness arising from inherent strength of polymers, Extreme Mechanics Letters 56 (2022) 101819. doi:10.1016/j.eml.2022.101819.

[9] Z. Fan, S.-Q. Wang, Resolving stress state at crack tip to elucidate nature of elastomeric fracture, Extreme Mechanics Letters 61 (2023) 101986. doi:10.1016/j.eml.2023.101986.

[10] F. Bueche, Tensile strength of rubbers, Journal of Polymer Science 24 (106) (1957) 189–200. doi:10.1002/pol.1957.1202410603.

[11] D. E. Hanson, J. L. Barber, The theoretical strength of rubber: Numerical simulations of polyisoprene networks at high tensile strains evidence the role of average chain tortuosity, Modelling and Simulation in Materials Science and Engineering 21 (7) (2013) 075013. doi:10.1088/0965-0393/21/7/075013.

[12] R. Hentschke, Tensile strength of rubber described via the formation and rupture of load-bearing polymer chains, Physical Review E 106 (1) (2022) 014505. doi:10.1103/PhysRevE.106.014505.

[13] M. Tehrani, A. S. Sarvestani, Effect of chain length distribution on mechanical behavior of polymeric networks, European Polymer Journal 87 (2017) 136–146. doi:10.1016/j.eurpolymj.2016.12.017.

[14] A. Arora, T.-S. Lin, H. K. Beech, H. Mochigase, R. Wang, B. D. Olsen, Fracture of polymer networks containing topological defects, Macromolecules 53 (17) (2020) 7346–7355.

[15] C. W. Barney, Z. Ye, I. Sacligil, K. R. McLeod, H. Zhang, G. N. Tew, R. A. Riggleman, A. J. Crosby, Fracture of model end-linked networks, Proceedings of the National Academy of Sciences 119 (7) (2022) e2112389119. doi:10.1073/pnas.2112389119.

[16] F. J. Vernerey, R. Brighenti, R. Long, T. Shen, Statistical damage mechanics of polymer networks, Macromolecules 51 (17) (2018) 6609–6622. doi:10.1021/acs.macromol.8b01052.

[17] M. R. Buche, M. N. Silberstein, Chain breaking in the statistical mechanical constitutive theory of polymer networks, Journal of the Mechanics and Physics of Solids 156 (2021) 104593. doi:10.1016/j.jmps.2021.104593.

[18] M. Tao, S. Lavoie, Z. Suo, M. K. Cameron, The effect of scatter of polymer chain length on strength, Extreme Mechanics Letters 61 (2023) 102024.

[19] A. Arora, T.-S. Lin, B. D. Olsen, Coarse-grained simulations for fracture of polymer networks: Stress versus topological inhomogeneities, Macromolecules 55 (1) (2021) 4–14.

[20] A. Arora, Effect of spatial heterogeneity on the elasticity and fracture of polymer networks, Macromolecules 58 (2) (2024) 1143–1155.

[21] J. Lei, Z. Li, S. Xu, A mesoscopic network mechanics method to reproduce the large deformation and fracture process of cross-linked elastomers, Journal of the Mechanics and Physics of Solids 156 (2021) 104599. doi:10.1016/j.jmps.2021.104599.

[22] P. J. Flory, N. Rabjohn, M. C. Shaffer, Dependence of elastic properties of vulcanized rubber on the degree of cross linking, Journal of Polymer Science 4 (3) (1949) 225–245.

[23] G. Taylor, S. Darin, The tensile strength of elastomers, Journal of Polymer Science 17 (86) (1955) 511–525.

[24] T. J. Dudek, F. Bueche, Tensile strength of gum and reinforced EPR and SBR vulcanizates, Journal of Applied Polymer Science 8 (2) (1964) 555–564. doi:10.1002/app.1964.070080202.

[25] C. M. Kok, V. H. Yee, The effects of crosslink density and crosslink type on the tensile and tear strengths of NR, SBR and EPDM gum vulcanizates, European Polymer Journal 22 (4) (1986) 341–345. doi:10.1016/0014-3057(86)90203-X.

[26] J. Kim, G. Zhang, M. Shi, Z. Suo, Fracture, fatigue, and friction of polymers in which entanglements greatly outnumber cross-links, Science 374 (6564) (2021) 212–216.

[27] H. Tsukeshiba, M. Huang, Y.-H. Na, T. Kurokawa, R. Kuwabara, Y. Tanaka, H. Furukawa, Y. Osada, J. P. Gong, Effect of polymer entanglement on the toughening of double network hydrogels, The Journal of Physical Chemistry B 109 (34) (2005) 16304–16309. doi:10.1021/jp052419n.

[28] D. Zheng, S. Lin, J. Ni, X. Zhao, Fracture and fatigue of entangled and unentangled polymer networks, Extreme Mechanics Letters 51 (2022) 101608. doi:10.1016/j.eml.2022.101608.

[29] R. Zhu, D. Zhu, Z. Zheng, X. Wang, Tough double network hydrogels with rapid self-reinforcement and low hysteresis based on highly entangled networks, Nature Communications 15 (2024) 1344. doi:10.1038/s41467-024-45485-8.

[30] D. Zhong, Z. Wang, J. Xu, J. Liu, R. Xiao, S. Qu, W. Yang, A strategy for tough and fatigue-resistant hydrogels via loose cross-linking and dense dehydration-induced entanglements, Nature Communications 15 (2024) 5896. doi:10.1038/s41467-024-50364-3.

[31] C. Yang, T. Yin, Z. Suo, Polyacrylamide hydrogels. i. network imperfection, Journal of the Mechanics and Physics of Solids 131 (2019) 43–55.

[32] Y. Mao, B. Talamini, L. Anand, Rupture of polymers by chain scission, Extreme Mechanics Letters 13 (2017) 17–24. doi:10.1016/j.eml.2017.01.003.

[33] Y. Mao, L. Anand, A theory for fracture of polymeric gels, Journal of the Mechanics and Physics of Solids 115 (2018) 30–53. doi:10.1016/j.jmps.2018.02.008.

[34] B. Li, N. Bouklas, A variational phase-field model for brittle fracture in polydisperse elastomer networks, International Journal of Solids and Structures 182–183 (2020) 193–204. doi:10.1016/j.ijsolstr.2019.08.012.

[35] D. Mukherji, C. F. Abrams, Mechanical behavior of highly cross-linked polymer networks and its links to microscopic structure, Physical Review E 79 (2009) 061802. doi:10.1103/PhysRevE.79.061802.

[36] Y. Higuchi, K. Saito, T. Sakai, J. P. Gong, M. Kubo, Fracture process of double-network gels by coarse-grained molecular dynamics simulation, Macromolecules 51 (8) (2018) 3075–3087. doi:10.1021/acs.macromol.8b00124.

[37] S. Mohanty, J. Blanchet, Z. Suo, W. Cai, Why is the strength of an elastomeric polymer network so low, npj Computational Materials 12 (2026) 269.

[38] R. J. Wagner, E. Hobbs, F. J. Vernerey, A network model of transient polymers: exploring the micromechanics of nonlinear viscoelasticity, Soft Matter 17 (38) (2021) 8742–8757.

[39] R. J. Wagner, J. Dai, X. Su, F. J. Vernerey, A mesoscale model for the micromechanical study of gels, Journal of the Mechanics and Physics of Solids 167 (2022) 104982.

[40] J. Tauber, L. Rovigatti, S. Dussi, J. van der Gucht, Sharing the load: Stress redistribution governs fracture of polymer double networks, Macromolecules 54 (18) (2021) 8563–8574. doi:10.1021/acs.macromol.1c01275.

[41] S. Assadi, S. C. Lamont, N. Hansoge, Z. Liu, V. Crespo-Cuevas, F. Salmon, F. J. Vernerey, Nonaffine motion and network reorganization in entangled polymer networks, Soft Matter 21 (11) (2025) 2096–2113.

[42] J. Huang, J. Liu, S. Lin, Topological mechanics of entangled networks, arXiv preprint arXiv:2509.17813 (2025).

[43] B. Mottaqin, B. Morrow, R. J. Wagner, Physically-motivated primitive path analysis of entangled polymer networks, arXiv preprint arXiv:2606.02174 (2026).

[44] T. Uneyama, Y. Masubuchi, Multi-chain slip-spring model for entangled polymer dynamics, The Journal of chemical physics 137 (15) (2012) 154902.

[45] A. E. Likhtman, Single-chain slip-link model of entangled polymers: Simultaneous description of neutron spin- echo, rheology, and diffusion, Macromolecules 38 (14) (2005) 6128–6139.

[46] W. Kuhn, F. Grün, Beziehungen zwischen elastischen konstanten und dehnungsdoppelbrechung hochelastischer stoffe, Kolloid-Zeitschrift 101 (3) (1942) 248–271. doi:10.1007/BF01793684.

[47] A. Cohen, A padé approximant to the inverse langevin function, Rheologica Acta 30 (1991) 270–273. doi:10.1007/BF00366640.

[48] G. V. Schulz, Über die kinetik der kettenpolymerisationen. v., Zeitschrift für Physikalische Chemie 43B (1) (1939) 25–46. doi:10.1515/zpch-1939-4304.

[49] IUPAC, Schulz–zimm distribution, Compendium of Chemical Terminology, the Gold Book. doi:10.1351/goldbook.S05502.

[50] M. Rubinstein, R. H. Colby, Polymer Physics, Oxford University Press, Oxford, 2003.

[51] Y.-H. Zang, P. J. Carreau, A correlation between critical end-to-end distance for entanglements and molecular chain diameter of polymers, Journal of applied polymer science 42 (7) (1991) 1965–1968.